Scientific Research Publishing

Journal of High Energy Physics, Gravitation and Cosmology, 2026, 12(1), 431-470
https://www.scirp.org/journal/jhepgc
ISSN Online: 2380-4335
ISSN Print: 2380-4327

Galactic Rotation Curves Explained in the 4DEU Framework by 3D Spatial Curvature from Local Gravitational Blocking of Cosmic Expansion: No Need for Dark Matter

Domenico Maglione

Technical Operations Department, Special Product's Line S.p.A., Anagni, Italy
Email: maglioned@libero.it

How to cite this paper: Maglione, D. (2026) Galactic Rotation Curves Explained in the 4DEU Framework by 3D Spatial Curvature from Local Gravitational Blocking of Cosmic Expansion: No Need for Dark Matter. *Journal of High Energy Physics, Gravitation and Cosmology*, **12**, 431-470.
https://doi.org/10.4236/jhepgc.2026.121025

Received: November 10, 2025
Accepted: January 20, 2026
Published: January 23, 2026

Abstract

The observed near flatness of galactic rotation curves has long been interpreted as evidence for large amounts of non-baryonic dark matter. Here we show that this phenomenon can be fully explained within the Four-Dimensional Electromagnetic Universe (4DEU) theory. In this framework, gravitation arises from curvature confined to the three-dimensional (3D) spatial hypersurface of a four-dimensional (4D) universe. The so-called "dark halo" does not correspond to any new form of matter but to the intrinsic 3D spatial curvature produced by the gravitational constraint that locally blocks only the 3D component of the 4D cosmic expansion within gravitationally bound systems. Using a Hamiltonian formulation restricted to static spatial slicing (vanishing extrinsic curvature), the **effective density** sourcing the curvature naturally separates into a baryonic term and an additional geometric contribution associated with the constraint. To test this hypothesis quantitatively, we analyzed the rotation curves from the entire SPARC database, selecting the 129 galaxies that satisfy the statistical and physical quality criteria defined in the method section. The extra-velocity component $v_{\text{extra}} = \sqrt{v_{\text{obs}}^2 - v_{\text{bar}}^2}$ was fitted in log-log space with the relation $v_{\text{cve}}(r) = V_0 (r/R_{\text{ref}})^{\varepsilon/2}$, where $v_{\text{cve}}(r)$ denotes the extra velocity component predicted by the 4DEU model, corresponding to the extra-baryonic curvature term that replaces dark matter in ΛCDM. V_0 represents the characteristic velocity at the reference radius R_{ref}, and ε is the radial-flexibility parameter quantifying incomplete blocking of the 3D-only cosmic expansion in the outermost regions. Model parameters were obtained via **weighted least-squares**, and their statistical consistency was assessed through χ^2, and p-value evaluation in logarithmic

space. Out of the 129 SPARC galaxies that met the selection criteria, 128 yielded statistically consistent fits ($p \geq 0.01$), demonstrating that their outer rotation curves are quantitatively reproduced by the curvature-from-gravitational-constraint mechanism alone, without invoking dark matter, modified gravity, or any additional hypothesis. These results provide strong empirical support for the view that the apparent dark halos are a manifestation of 3D spatial curvature induced by the local suppression of 3D-only cosmic expansion, not by new particles. The 4DEU theoretical framework therefore offers a unified and parameter-free geometric explanation of galactic dynamics consistent with observational data across the SPARC sample.

Keywords

Dark Matter Problem, Four-Dimensional Electromagnetic Universe (4DEU), Galaxy Rotation Curves Fitting, SPARC Database, Gravitational Constraint, Dark Halo as Spatial Curvature

1. Introduction

1.1. Why Dark Matter Was Hypothesized

The persistent flatness of spiral-galaxy rotation curves beyond the optical disk was the earliest systematic hint of an unseen gravitating component [1]. Pioneering H I/Hα kinematics and meta-analyses established that orbital speeds remain roughly constant to large radii, inconsistent with the Keplerian fall-off expected from the observed baryonic mass alone. Modern compilations such as SPARC (175 disks with accurate rotation curves and 3.6 μm photometry) cement this empirical picture across a wide dynamic range [2] [3].

Independent and complementary evidence comes from gravitational lensing. Mass reconstructions of merging clusters (e.g., the Bullet Cluster) show a clear separation between the baryonic plasma (X-ray) and the total gravitational potential traced by lensing—strongly suggesting a dominant, non-luminous component [4]. More broadly, weak-lensing surveys and theory reviews have developed lensing as a precision mass probe from galaxy to cosmic-web scales [5] [6].

On cosmological scales, the CMB anisotropies and large-scale structure require a cold, pressureless matter component (with density parameter defined as $\Omega_c = \rho_c / \rho_{\text{crit}}$) to fit the observed acoustic peaks and growth history, yielding precise constraints on the physical density $\Omega_c h^2$ that underpin the ΛCDM model. The Planck 2018/2020 parameter analysis remains the standard reference for these inferences [7].

Decades of theory and experiment have proposed candidates and searched for them without definitive detection [8] [9]. Leading paradigms include WIMPs, axions/ALPs, and sterile neutrinos; comprehensive reviews summarize their motivations and constraints. State-of-the-art direct-detection experiments such as XENONnT and LZ have reported world-leading null results, pushing spin-in-

decpendent WIMP-nucleon cross-section limits to unprecedented depths. Thus, despite sustained progress since the 1930s, the fundamental nature of "dark matter" remains unknown [10]-[12].

In view of this persistent impasse, alternative theoretical approaches have been explored in recent years. Among these, the Four-Dimensional Electromagnetic Universe (4DEU) theory represents a recent development, still relatively unfamiliar within academic research in cosmology and gravitational physics. A more extensive introductory overview is therefore provided below, summarizing its essential assumptions and predictions and establishing the conceptual background for the subsequent quantitative analysis of galaxy rotation curves.

1.2. A Comprehensive Overview of the 4DEU Framework

The Four-Dimensional Electromagnetic Universe (4DEU) model postulates the cosmos is a ***real four-dimensional Euclidean hypersphere*** composed entirely of genuine spatial coordinates, rather than as a (3 + 1)-dimensional spacetime in which time acts as an abstract parameter (Postulate 1 in [13]). In this picture, the global evolution of the Universe corresponds to a uniform geometric expansion along the fourth spatial coordinate—here denoted T—proceeding at the constant rate c. Within the 4DEU theoretical framework, the constant c is not interpreted as a velocity in the conventional relativistic sense; instead, it represents the expansion rate of the real-time dimension and, more fundamentally, a universal conversion factor linking the spatial and temporal units traditionally adopted in physics.

Since in 4DEU all four coordinates are real spatial dimensions, the universe constitutes a real four-dimensional hypersphere. By definition, any real hyperspherical geometry possesses a well-defined geometric center, corresponding to the origin of expansion—the event conventionally identified as the Big Bang. This central point provides a privileged reference frame from which the hyperspherical radius grows uniformly. In this respect, the Big Bang in 4DEU fulfills a role analogous to that of the cosmic microwave background (CMB) rest frame in ΛCDM cosmology.

An additional consequence of this model is that the 4D Universe possesses a radius R defined along the real-time dimension (the fourth spatial dimension), which increases with cosmic expansion according to the simple relation $R = ct$.

Another fundamental difference between the treatment of time in Relativity and in the 4DEU framework lies in its mathematical nature. In Minkowski spacetime, the temporal coordinate enters the metric through an imaginary term $ic\mathrm{d}t$, so that its square contributes negatively to the spacetime interval, as $-(c\mathrm{d}t)^2$. The resulting spacetime interval

$$\mathrm{d}s^2 = (\mathrm{d}x)^2 + (\mathrm{d}y)^2 + (\mathrm{d}z)^2 - (c\,\mathrm{d}T)^2$$

defines a pseudo-Euclidean geometry in which time is not a real spatial dimension but an imaginary one, distinct in sign and meaning from the three spatial coordi-

nates. In the 4DEU framework, by contrast, the temporal coordinate T represents a genuine spatial dimension of the four-dimensional Euclidean hypersphere, which, according to the Restricted Holographic Principle (see below; Postulate 2 in [13]), appears to observers confined within its three-dimensional portion as the flow of time. The corresponding interval is

$$\mathrm{d}s^2 = (\mathrm{d}x)^2 + (\mathrm{d}y)^2 + (\mathrm{d}z)^2 + (c\,\mathrm{d}T)^2$$

where the term $(c\,\mathrm{d}T)^2$ is real and positive. Thus, the global geometry of the Universe is strictly Euclidean, and what we perceive as the passage of time corresponds, in geometric terms, to the uniform expansion of the Universe at the constant rate c along this real fourth spatial dimension.

The three familiar dimensions thus form a three-dimensional hypersurface (a 3-sphere) embedded in this four-dimensional geometry where observers, measuring devices, and all physical interactions are fully confined. The fourth coordinate is orthogonal to this surface and cannot be directly accessed; its steady expansion at rate c is perceived by 3D observers as the continuous **flow of time**. Consequently, the temporal evolution we register in physical processes corresponds to the uniform expansion of the Universe at the constant rate c along its real fourth spatial dimension T.

As already mentioned, the 4DEU Theory rests on a second fundamental postulate, the Restricted Holographic Principle (RHP). This postulate asserts that any phenomenon occurring along the fourth spatial dimension cannot be directly observed, but manifests within the three-dimensional hypersurface where observers reside, in a qualitatively transformed yet quantitatively proportional manner.

Another key postulate of the 4DEU Theory (Postulate 3) states the existence and nature of Temporal Waves (TWs): stationary electromagnetic waves confined exclusively to the fourth spatial dimension, each characterized by a wavelength

$$\lambda_{tw} = 4R_T$$

and energy

$$E_{\mathrm{tw}(R_T)} = hf_{\mathrm{tw}(R_T)} = \frac{hc}{\lambda_{\mathrm{tw}(R_T)}}$$

Here $E_{\mathrm{tw}(R_T)}$ denotes the Energy of a TW when the radius of the 4D universe equals R_T, h is Planck's constant; and $f_{\mathrm{tw}(R_T)}$ and $\lambda_{\mathrm{tw}(R_T)}$ are, respectively, the frequency and wavelength of a TW at epoch when the radius of the 4D universe is R_T ([13] [14] and see **Figure 1** in [15]).

Physical observables such as mass, energy, electric charge, magnetic poles, and even gravity emerge as consequences of the Restricted Holographic Principle (RHP), which can be interpreted as three-dimensional projections of these fundamental waves.

Consequences of the Restricted Holographic Principle (RHP)

From the Restricted Holographic Principle, the following physical interpretations arise:

Mass

The energy of the Temporal Waves (TWs) appears qualitatively different within the 3D part of the 4D Universe where we live, manifesting as *mass*. Quantitatively, this correspondence follows the well-known proportional relation:

$$E = mc^2$$

Electric and Magnetic Charge

According to the 4DEU framework, there exist two types of TWs with opposite phases (0 and π). Based on the RHP, these two phases manifest in the 3D portion of the Universe, where observers reside, *qualitatively* as positive electric charge and north magnetic pole, or negative electric charge and south magnetic pole, respectively. Quantitatively, the corresponding electric and magnetic field components are described by the following expressions:

$$E_{\mathrm{tw}(x,R_T)} = \pm E_{0\left[\mathrm{tw}(R_T)\right]} \sin\left(\frac{\pi x}{2R_T}\right)$$

and

$$B_{\mathrm{tw}(x,R_T)} = \pm B_{0\left[\mathrm{tw}(R_T)\right]} \sin\left(\frac{\pi x}{2R_T}\right)$$

where x denotes a position along the real-time dimension, and ranging from the privileged coordinates $-R_T$ to $+R_T$ (R_T is the radius of 4D universe and its 3D portion); $E_{\mathrm{tw}(x,R_T)}$ indicate the intensity of the electric field of a TW at point x (along the diameter $2R_T$ of the 4D universe), and $E_{0\left[\mathrm{tw}(R_T)\right]}$ denotes the maximum absolute amplitude of the electric field. $B_{0\left[\mathrm{tw}(R_T)\right]}$ represent the maximum absolute amplitude of the magnetic field.

Passage of Time and Galaxy Recession

According to the Restricted Holographic Principle (RHP), every physical process occurring along the fourth real spatial dimension has a corresponding counterpart within the observable three-dimensional part of the 4D Universe, characterized by a qualitative manifestation (how it is perceived) and a quantitative relation (how it is measured).

The uniform expansion along the fourth dimension manifests qualitatively as the *flow of time* and is quantitatively described by the fundamental relation $R_T = cT$. The same expansion in the 3D part of the 4D Universe appears qualitatively as the **mutual recession of gravitationally unbound galaxies**, and quantitatively it is expressed by the **Hubble parameter** according to the 4DEU law [15]:

$$H(z) = H_0(1+z)$$

In other words, the real 4D expansion that gives rise to the passage of time is perceived, within the 3D hypersurface, as the observable cosmic expansion: the advance of time in 4D corresponds to the increasing separation of galaxies in 3D.

Dark Energy

TWs generate a radially directed radiation pressure that acts perpendicularly to the 3D hypersurface, driving the uniform expansion at rate c. According to the

Restricted Holographic Principle (RHP), this negative radiation pressure naturally replaces the role of dark energy in the ΛCDM framework, eliminating the need for any external cosmological constant or exotic field. Quantitatively, this pressure—defined as a 3*D pressure* because it acts not on a two-dimensional surface but on the three-dimensional hypersurface of the 4D Universe—is given by:

$$\Pi_{\mathrm{tw}(R_T)} = -\frac{hc}{8\pi^2 R_T^5}$$

where $\Pi_{\mathrm{tw}(R_T)}$ indicates the 3D pressure of a single TW when the radius of the 4D universe is R_T.

Therefore, within the 4DEU theoretical framework, the driving mechanism of cosmic expansion is the 3D radiation pressure of the TWs acting perpendicularly to the 3D section of the 4D Universe.

In the same theoretical context, the apparent late-time acceleration of the Universe—observed at low redshifts through measurements of the Hubble parameter $H(z)$ and type Ia supernova luminosity distances—requires no dark-energy component, being fully explained by the intrinsic geometry of the 4DEU framework.

In the standard matter-dominated Friedmann model without a cosmological constant, the expansion rate was predicted to follow equation:

$$H(z) = H_0 (1+z)^{3/2}$$

implying a continuously decelerating universe. However, the observed $H(z)$ data exhibited a slower decline, inconsistent with this prediction, and could be reproduced only by introducing a dark-energy component with negative pressure.

In contrast, within the 4DEU framework, the relation between H and z is strictly linear:

$$H(z) = H_0 (1+z)$$

A recent study [15] demonstrated that this linear relation fully accounts for the observed low-redshift behavior of the Hubble parameter without invoking dark energy.

The apparent late-time acceleration of cosmic expansion emerges naturally as a projection effect of uniform four-dimensional expansion onto the three-dimensional hypersurface where observations are performed.

The results of that study show that the linear 4DEU prediction for $H(z)$ accurately reproduces model-independent data from Type Ia supernovae and cosmic chronometers with a high level of statistical significance.

In particular, the statistical consistency is markedly higher when adopting the Planck-CMB determination of the Hubble constant ($H_0 = 67.4\ \mathrm{km \cdot s^{-1} \cdot Mpc^{-1}}$) than when using the local distance-ladder estimate ($H_0 \approx 73\ \mathrm{km \cdot s^{-1} \cdot Mpc^{-1}}$), with a likelihood ratio of about 219:1 in favor of the Planck-CMB value.

This behavior indicates that the value near $67.4\ \mathrm{km \cdot s^{-1} \cdot Mpc^{-1}}$ should be regarded as the physically meaningful one, while the higher local values may be af-

fected by systematics that are not yet fully understood.

Within the 4DEU framework, the observed late-time acceleration of the Universe therefore requires no dark-energy component, as it naturally arises from the intrinsic geometry of uniform four-dimensional expansion.

Gravity

According to the Restricted Holographic Principle (RHP), regions within the 3D part of the four-dimensional Universe that possess a higher density of Temporal Waves (TWs) correspond to 3D zones of greater mass. This implies that, in such regions, TWs exert a locally stronger radiation pressure than in adjacent areas of lower density (or with no mass), thereby generating a differential pressure field. **Qualitatively, this differential pressure manifests to 3D observers as gravitation, arising from a purely spatial (3D) curvature rather than a spacetime curvature as in General Relativity.** Quantitatively, in the weak-field regime, this curvature is described by the metric:

$$ds_{3D}^2 = \frac{dr^2}{1-\frac{2GM}{c^2 r}} + r^2 d\Omega_2^2$$

Therefore, in the 4DEU framework, gravitation arises exclusively from the curvature of the three-dimensional hypersurface, whereas the fourth dimension remains flat. In the weak-field limit, this purely spatial curvature reproduces the classical relativistic effects—gravitational redshift, light deflection, Shapiro delay, and Mercury's perihelion precession—confirming full empirical consistency [16].

Internal Polarization Quantization of Temporal Waves and the Emergence of Particle Spin

In the context of this comprehensive overview of the 4DEU theoretical framework, it is useful to examine how the polarization of Temporal Waves (TWs), when **interpreted** through the Restricted Holographic Principle (RHP), manifests to observers confined to the 3D portion of the 4D Universe as the intrinsic spins of elementary particles. This constitutes **Corollary 4 of Postulate 2 (RHP)** within the 4DEU theory. In analogy with the already established correspondences—where mass, electric charge, and 3D spatial curvature arise from different aspects of TW structure—the quantization of the **internal circular polarization angle** corresponds to the **various spin states** observed in the 3D portion of the 4D Universe.

In the RHP formulation, each fundamental property of a TW has a specific counterpart in the observable 3D section of the 4D Universe: the energy of TWs appears as mass, their phase as electric charge, and their density as 3D spatial curvature. Likewise, TWs possess an intrinsic electromagnetic polarization plane, associated with the oscillatory behavior of their electric and magnetic fields along the real fourth spatial dimension, around T-axis.

Therefore, **Corollary 4 states that** *the internal circular polarization angle of a TW can assume only quantized values in units of* π/2, *giving rise, within the* 3*D portion of the* 4*D Universe where observers reside, to different intrinsic spin states.*

This leads to the following correspondence:

$$\theta_{\text{pol}} \in \left\{\frac{\pi}{2}, \pi, \frac{3\pi}{2}, 2\pi\right\} \quad \rightarrow \quad \text{Spin} \in \left\{0, \frac{1}{2}, 1, 2\right\}$$

where θ_{pol} denotes the internal circular polarization angle of a Temporal Wave (TW).

In this interpretation, the quantized internal circular polarization angle of a Temporal Wave (TW) appears, within the 3D portion of the 4D Universe where observers reside, as the different intrinsic spin states of elementary particles. More precisely:

- **Spin 0** corresponds to a TW with a polarization angle $\theta_{\text{pol}} = \pi/2$,
- **Spin 1/2** corresponds to $\theta_{\text{pol}} = \pi$.
- **Spin 1** corresponds to $\theta_{\text{pol}} = 3\pi/2$.
- **Spin 2** corresponds to a full 2π polarization cycle ($\theta_{\text{pol}} = 0$ or 2π).

All these configurations return to their initial state after a full 2π rotation.

Thus, through Corollary 4 of the Restricted Holographic Principle (RHP), the 4DEU theory can account for the full set of particle spin states without introducing additional quantum fields or new degrees of freedom, thereby strengthening its interpretative coherence from microscopic to cosmological scales.

1.3. Observational Validation of the 4DEU Predictions

The Four-Dimensional Electromagnetic Universe (4DEU) theoretical framework provides a set of independent quantitative predictions that are in remarkable agreement with observational data across several domains of modern cosmology. These include:

- **Consistency with weak-field gravitational tests**, Full agreement with weak-field gravitational tests, as the 4DEU framework leads to exactly the same analytical expressions for gravitational redshift, light deflection, Shapiro delay, and perihelion precession as those obtained in General Relativity [16];
- **Agreement with model-independent determinations of** H_z at different redshifts, without requiring a dark-energy component, through the linear relation $H_z = H_0(1+z)$ [15];
- **Consistency with the observationally determined temperature of the cosmic microwave background (CMB)** at different redshifts, as predicted from the thermodynamic equations derived within 4DEU [14] [17].

The third point listed above is examined in greater detail below.

According to the thermodynamic formulation of the 4DEU Universe, the absolute temperature T of the radiation field is expressed as:

$$Tem_z = (1+z)Tem_0$$

where Tem_0 denotes present CMBR temperature (≈2.725 K) and Tem_z that at redshift z (Equation B.3.1 derived from Eq.46 in [17]).

This relation indicates that the Cosmic Microwave Background (CMB) temperature scales linearly with redshift, a behavior that follows directly from the 4DEU geometry and requires no additional assumptions.

Observational data at $z = 0.89$, $z = 3.025$, and $z = 6.34$ ([18]-[20]) are in excellent agreement with these predictions, confirming the linear dependence of the CMB temperature on redshift within the reported uncertainties [17].

In addition, the 4DEU framework naturally accounts for the unexpectedly advanced properties of the earliest galaxies observed by JWST and HST at $z > 10$. In this model, the privileged time T_z follows the same linear dependence on redshift as other cosmological quantities,

$$T_z = T_0 (1+z)^{-1}$$

where T_0 represents the present age of the Universe in the 4DEU framework ($T_0 \approx (14.51 \pm 0.011)$ Gyr).

This relation implies that cosmic epochs corresponding to high redshifts are substantially older when expressed in privileged time than when evaluated in the ΛCDM cosmic timescale. Consequently, the galaxies **GN-z11** [21], **GS-z12** [22], and **JADES-GS-z14-0** [23] appear approximately three times older than predicted by ΛCDM—fully consistent with their observed level of chemical enrichment and structural evolution [14].

Together, these results demonstrate that the 4DEU framework not only reproduces the classical weak-field tests of General Relativity but also quantitatively matches modern cosmological observations—including the evolution of H_z, CMB temperature evolution, and early-galaxy formation—without invoking dark matter, dark energy, or any additional cosmological parameters.

The aim of this work is to test whether the application of the 4DEU framework can account for the observed galactic rotation curves without the need for dark matter.

Interpreted within 4DEU, the "dark halo" that reproduces these outer rotation curves corresponds not to new particles, but to **intrinsic 3D spatial curvature** induced by the **gravitational constraint that locally blocks the 3D component of the cosmic expansion**—with associated Ricci scalar consistent with the inferred effective densities in the halo regime. In the present work, this hypothesis is tested across the entire SPARC galaxy catalogue [2] [3], selecting the **129 galaxies** that satisfy the statistical and physical quality criteria defined in the Methods section, confirming that their observed rotation curves can be quantitatively reproduced without invoking any form of dark matter.

The following sections test this geometric interpretation quantitatively by applying the 4DEU kinematic law to the full SPARC galaxy sample.

2. Base Hypothesis: The Gravitational Constraint Locally Blocking the 3D-Only Cosmic Expansion

Within the 4DEU theoretical framework, the phenomenon conventionally attributed to dark matter is interpreted as a purely geometric effect arising from the gravitational constraint that locally halts the 3D-only cosmic expansion. It therefore constitutes the central working hypothesis of the present study.

This constraint, hereafter referred to as the **G**ravitational **C**onstraint that **L**ocally **B**locks 3D-only cosmic **E**xpansion **(GCLBE)**, prevents the spatial separation of gravitationally bound masses within galaxies that would otherwise drift apart following the 3D-only cosmic expansion. The effect of this constraint is "*geometrically stored*" in the form of intrinsic curvature of the three-dimensional hypersurface (purely 3D), rather than as an additional form of matter (such as dark matter).

A qualitative analogy is shown in Figure 1: when a rigid wire connects two points on the surface of an inflating balloon, it limits the local expansion and induces an inward curvature of the membrane. Similarly, in 4DEU, the gravitational constraint acts within gravitationally bound systems—such as stellar systems, galaxies, and clusters—producing local spatial curvature that, in the standard ΛCDM interpretation, is "*mistaken*" for the presence of dark matter.

This geometric interpretation can be mathematically formulated more rigorously by adopting a 3 + 1 decomposition applied to a purely spatial geometry.

In the 4DEU framework, the real-time dimension T remains flat, while all gravitational effects are encoded in the intrinsic curvature of the three-dimensional hypersurface—which represents the static spatial section of the 4D hypersphere, not a surface embedded in a higher-dimensional space. In the static-slicing limit, where the extrinsic curvature vanishes ($K_{ij}=0$), reflecting the absence of local geometric evolution along the fourth spatial dimension and thereby reducing the Hamiltonian constraint to a direct correspondence between the three-dimensional Ricci scalar and an **effective density** term:

$$^{(3)}R=\frac{16\pi G}{c^2}\rho_{\text{eff}} \tag{1}$$

In the 4DEU framework, this effective density does not represent real matter density but quantifies the amount of spatial curvature induced by both the baryonic mass distribution and the local blocking only the 3D cosmic expansion:

$$\rho_{\text{eff}}(r)=\rho_b(r)+\rho_{\text{cve}}(r) \tag{2}$$

where $\rho_b(r)$ is the observable baryonic component, and $\rho_{\text{cve}}(r)$ is the curvature-generated term associated with the GCLBE—the contribution that, in the standard interpretation, would be ascribed to dark matter. For clarity, the subscript "**cve**" denotes the ***Constraint-Velocity contribution to cosmic Expansion*** **(CVE)**, corresponding to the curvature-induced extra velocity component that replaces dark matter in the ΛCDM framework.

In the weak-field, spherically symmetric regime, the effective density can be inferred directly from the observed rotational velocity profile $v(r)$:

$$\rho_{\text{eff}}(r)=\frac{1}{4\pi Gr^2}\frac{\mathrm{d}}{\mathrm{d}r}\left[rv^2(r)\right] \tag{3}$$

Equation (3) follows directly from the standard Newtonian description of circular motion under spherical symmetry (see, e.g., [24]), as shown below.

Starting from the balance between the centrifugal and gravitational accelerations,

Figure 1. Illustration of how a constraint affects the curvature of an expanding surface. The wire attached at two points limits expansion, causing an inward curvature of the balloon surface (reproduced from [14]).

$$\frac{v^2(r)}{r} = \frac{GM(r)}{r^2} \tag{3a}$$

where $v(r)$ is the observed circular velocity at radius r, $M(r)$ is the total (effective) mass enclosed within that radius, and G is the gravitational constant.

Equation (3a) represents the first of the two classical Newtonian relations (see, e.g., [24]).

The second relation expresses the local mass continuity in spherical symmetry,

$$\frac{\mathrm{d}M(r)}{\mathrm{d}r} = 4\pi r^2 \rho_{\mathrm{eff}}(r) \tag{3b}$$

where $\rho_{\mathrm{eff}}(r)$ denotes the effective density corresponding to the total gravitational source term.

Equations (3a) and (3b) together constitute the **two fundamental Newtonian equations** that connect the velocity profile $v(r)$, the enclosed mass $M(r)$, and the density distribution $\rho_{\mathrm{eff}}(r)$.

From Equation (3a) the enclosed mass can be written as:

$$M(r) = \frac{rv^2(r)}{G} \tag{3c}$$

Differentiating Equation (3c) with respect to r gives:

$$\frac{\mathrm{d}M(r)}{\mathrm{d}r} = \frac{1}{G}\frac{\mathrm{d}}{\mathrm{d}r}\left[rv^2(r)\right] \tag{3d}$$

Substituting Equation (3d) into the continuity relation (Equation (3b)) eliminates $M(r)$ and yields:

$$4\pi r^2 \rho_{\mathrm{eff}}(r) = \frac{1}{G}\frac{\mathrm{d}}{\mathrm{d}r}\left[rv^2(r)\right] \tag{3e}$$

Rearranging Equation (3e) yields Equation (3) exactly:

$$\rho_{\text{eff}}(r)=\frac{1}{4\pi G r^2}\frac{\mathrm{d}}{\mathrm{d}r}\left[rv^2(r)\right]$$

This derivation shows explicitly that Equation (3) is not an assumption but a direct consequence of the classical Newtonian relations, rewritten in geometric form to express the effective density purely in terms of the observable rotational velocity profile $v(r)$.

Equation (3), and its expanded form Equation (3f) (see below), are purely kinematic and model independent. In the outer regions of disk galaxies, the observed rotation curve typically becomes nearly flat, so that the total velocity profile (baryonic plus extra components) approaches a constant value $V_{0,\text{tot}}$, which is the asymptotic plateau of the total observed velocity $v(r)$. This means that $v(r)\simeq V_{0,\text{tot}}$ and its radial derivative tends to zero ($\mathrm{d}v/\mathrm{d}r\simeq 0$).

To make the dependence on $v(r)$ explicit, the derivative in Equation (3) can be expanded as follows:

$$\rho_{\text{eff}}(r)=\frac{1}{4\pi G r^2}\left[v^2(r)+2rv(r)\frac{\mathrm{d}v(r)}{\mathrm{d}r}\right] \tag{3f}$$

Under this condition, Equation (3f) simplifies to the isothermal-like form

$$\rho_{\text{eff}}(r)\simeq\frac{V_{0,\text{tot}}^2}{4\pi G r^2} \tag{4}$$

where $V_{0,\text{tot}}$ is the asymptotic plateau of the total observed velocity $v(r)$.

Equation (4) corresponds to a purely geometric curvature profile capable of sustaining a flat rotation curve without any dark-matter halo.

Finally, for completeness, an equivalent and fully model-independent derivation of Equation (3), based on Gauss's law under spherical symmetry, is provided in Appendix A.

3. Derivation of the 4DEU Equation for Extra Velocity Component

In the weak-field regime with effective spherical symmetry, the observed circular speed decomposes as the quadrature sum of baryonic terms and an additional component (extra component):

$$v_{\text{obs}}^2(r)=v_{\text{bulge}}^2(r)+v_{\text{disk}}^2(r)+v_{\text{gas}}^2(r)+v_{\text{extra}}^2(r) \tag{5}$$

Within 4DEU, as discussed before, the extra term is not attributed to dark matter but to the curvature generated by the gravitational constraint that locally blocks the 3D-only cosmic expansion (GCLBE). We model this contribution with a function $v_{\text{cve}}(r)$ that is fitted to the empirically inferred $v_{\text{extra}}(r)$. For compactness below, set $v\equiv v_{\text{cve}}$. As recalled in Section 2, the subscript *cve* denotes the **C**onstrain**t**-**V**elocity contribution to cosmic **E**xpansion **(CVE)**.

On the nearly flat outer segment—where v_{extra}^2 dominates, we assume that the logarithmic slope of the squared extra velocity is constant over the fitted radial

interval:

$$\frac{\mathrm{d}\ln v^2}{\mathrm{d}\ln r}=\varepsilon \tag{6}$$

where ε is a local radial-flexibility parameter (not universal), defined on the specific fitting range.

Using the chain rule,

$$\frac{\mathrm{d}\ln v^2}{\mathrm{d}\ln r}=\left(\frac{1}{v^2}\frac{\mathrm{d}v^2}{\mathrm{d}r}\right)r=2\frac{\mathrm{d}\ln v}{\mathrm{d}\ln r} \tag{7}$$

Equation (6) becomes:

$$2\frac{\mathrm{d}\ln v}{\mathrm{d}\ln r}=\varepsilon \;\Rightarrow\; \frac{\mathrm{d}\ln v}{\mathrm{d}\ln r}=\frac{\varepsilon}{2} \tag{8}$$

Since $\mathrm{d}\left(\ln v\right)=\dfrac{\mathrm{d}v}{v}$ and $\mathrm{d}\left(\ln r\right)=\dfrac{\mathrm{d}r}{r}$, Equation (8) is equivalent to

$$\frac{\mathrm{d}v}{v}=\frac{\varepsilon}{2}\frac{\mathrm{d}r}{r} \tag{9}$$

We now integrate between a reference radius R_{ref} (chosen as the geometric mean of the fitted radii, ($R_{\mathrm{ref}}=\mathrm{e}^{\langle\ln r\rangle}$) and a generic radius r. Defining

$$V_0\equiv v\left(R_{\mathrm{ref}}\right) \tag{10}$$

the definite integral of Equation (9) yields

$$\int_{V_0}^{v(r)}\frac{\mathrm{d}v'}{v'}=\frac{\varepsilon}{2}\int_{R_{\mathrm{ref}}}^{r}\frac{\mathrm{d}r'}{r'}\Rightarrow\ln\left(\frac{v\left(r\right)}{V_0}\right)=\frac{\varepsilon}{2}\ln\left(\frac{r}{R_{\mathrm{ref}}}\right) \tag{11}$$

Exponentiating,

$$v\left(r\right)=V_0\left(\frac{r}{R_{\mathrm{ref}}}\right)^{\varepsilon/2} \tag{12}$$

Equation (12) is the 4DEU extra-velocity law used in the fits. Here V_0 and ε are free parameters estimated from data on the selected halo-dominated radial range; V_0 is the normalization of the extra component at R_{ref}. Note that V_0 is **not** the asymptotic plateau of the total observed curve (often denoted $V_{0,\mathrm{tot}}$); it refers solely to the CVE component.

Interpretation of ε:

- $\varepsilon=0$: $v_{\mathrm{cve}}\left(r\right)$ is exactly flat, providing a constant contribution that perfectly counterbalances the decline of the baryonic component and thus sustains a constant outer observed velocity.
- $\varepsilon>0$: $v_{\mathrm{cve}}\left(r\right)$ gently rises with radius, more than compensating the baryonic decline.
- $\varepsilon<0$: The modeled function $v_{\mathrm{cve}}\left(r\right)$ decreases with radius, only partially compensating the baryonic decline and producing an observed curve $v_{\mathrm{obs}}\left(r\right)$ that falls more slowly than the pure Keplerian decay. This behavior indicates that the extra component provides a gravitational contribution insufficient to

fully counterbalance the baryonic velocity decline in the outer regions yet still maintains a residual curvature strong enough to prevent a complete Keplerian drop.

Equation (12) provides a minimal, phenomenological description of the curvature-induced extra component required by the data, without invoking any additional matter species.

4. From Rotation Curves to Effective Density and 3D Spatial Curvature

To connect the kinematic model of Equation (12) to its physical and geometric meaning, we derive the corresponding effective density $\rho_{\text{eff}}(r)$, *i.e.*, the formal equivalent of a mass distribution that would sustain the same rotational kinematics as the observed velocity profile.

In the ΛCDM framework this quantity would be interpreted as the density of dark matter, whereas in 4DEU it is reformulated as the effective density produced by the Gravitational Constraint that Locally Blocks the 3D-only cosmic expansion.

4.1. From Effective Density to 3D Curvature in the 4DEU Framework

In the 4DEU framework, the outer-halo regime is dominated by the curvature-induced component $v_{\text{cve}}(r)$ given by Equation (12):

$$v_{\text{cve}}(r) = V_0 \left(\frac{r}{R_{\text{ref}}} \right)^{\varepsilon/2}$$

Its square is:

$$v_{\text{cve}}^2(r) = V_0^2 \left(\frac{r}{R_{\text{ref}}} \right)^{\varepsilon} \tag{13}$$

Differentiating Equation (13) with respect to r yields:

$$\frac{\mathrm{d}v_{\text{cve}}}{\mathrm{d}r} = \frac{\varepsilon}{2} \frac{v_{\text{cve}}(r)}{r} \tag{14}$$

Substituting Equation (14) into Equation (3f) gives the effective extra-density associated with the GCLBE:

$$\rho_{\text{cve}}(r) = \frac{1}{4\pi G r^2} \left[v_{\text{cve}}^2(r) + 2r\, v_{\text{cve}}(r) \left(\frac{\varepsilon}{2} \frac{v_{\text{cve}}(r)}{r} \right) \right] = \frac{(1+\varepsilon) v_{\text{cve}}^2(r)}{4\pi G r^2} \tag{15}$$

Replacing $v_{\text{cve}}^2(r)$ from Equation (13):

$$\rho_{\text{cve}}(r) = \frac{(1+\varepsilon) V_0^2}{4\pi G r^2} \left(\frac{r}{R_{\text{ref}}} \right)^{\varepsilon} \tag{16}$$

Equation (16) implies $\rho_{\text{cve}} \propto r^{\varepsilon-2}$.

The admissibility condition $\varepsilon > -1$ ensures $\rho_{\text{cve}} > 0$ throughout the fitted range.

Since all other quantities in Equation (16) are strictly positive for $r>0$, the sign of ρ_{cve} is determined solely by the factor $(1+\varepsilon)$. Therefore, the physical requirement of a positive effective density implies $1+\varepsilon>0$, *i.e.* $\varepsilon>-1$. As will be shown in the Results section, this condition is fully satisfied by all galaxies in the analyzed sample. In particular, the only systems yielding negative fitted slopes (NGC7793, with $\varepsilon=-0.3165$, and UGC02916, with $\varepsilon=-0.3311$; see **Table 1** and Section 6) still fulfil $\varepsilon>-1$, thus maintaining a strictly positive curvature-induced density throughout their fitted radial ranges; the corresponding rows in Table I are highlighted in bold.

Possible cases:

- $\varepsilon=0$: $\rho_{\mathrm{cve}}\propto r^{-2}$, the standard isothermal profile.
- $\varepsilon>0$: ρ_{cve} decreases more slowly than r^{-2}, giving a mildly rising $v(r)$.
- $-1<\varepsilon<0$: ρ_{cve} falls faster than r^{-2}, so the curvature contribution weakens outward and $\rho_{\mathrm{eff}}\to\rho_{\mathrm{b}}$ at large radii.

4.2. Derivation of the 3D Spatial Curvature from the Hamiltonian Constraint

Within the 3 + 1 ADM (*Arnowitt-Deser-Misner*) formalism [25], the Hamiltonian constraint reads:

$$^{(3)}R+K^2-K_{ij}K^{ij}=\frac{16\pi G}{c^2}\rho_{\mathrm{eff}}(r) \tag{17}$$

In this formulation, K_{ij} quantifies how each spatial slice changes along the real-time dimension T, *i.e.* its extrinsic curvature with respect to the 3 + 1 decomposition. Its trace is $K=\gamma^{ij}K_{ij}$; therefore, $K^2=K_{ij}K^{ij}$ only in the absence of temporal deformation, that is, when the geometry of the slice does not bend or evolve along T.

In the 4DEU framework, the real-time dimension T, which corresponds to the radial coordinate of the four-dimensional real universe and not to a dynamical time as in relativity, is perfectly flat. Within gravitationally bound systems where the GCLBE halts the 3D expansion, the spatial hypersurfaces, representing the 3D part of the 4D universe where we live, remain locally constant along T.

This represents a geometrically static configuration, in the same sense in which "static slicing" in the 3 + 1 formulation denotes the absence of metric evolution along the chosen coordinate direction. For such a configuration, $K_{ij}=0$ and consequently $K=0$. Hence all extrinsic-curvature terms vanish, and the relation reduces to:

$$^{(3)}R=\frac{16\pi G}{c^2}\rho_{\mathrm{eff}}(r) \tag{18}$$

This static-slicing condition applies locally within gravitationally bound systems, where the Gravitational Constraint (GCLBE) halts the 3D-only cosmic expansion. On cosmological scales, however, the 4DEU geometry admits a global evolution along the **real-time dimension** T at rate c; hence $K_{ij}=0$ represents the local static limit of the full expanding hyperspherical universe.

Substituting the equation binding $\rho_{\text{eff}}(r)$ (Equation (3f)) into Equation (18) gives the curvature directly in terms of the rotation curve:

$$^{(3)}R = \frac{4}{c^2 r^2}\left[v^2(r) + 2rv(r)\frac{\mathrm{d}v(r)}{\mathrm{d}r}\right] \tag{19}$$

In the outer galactic region, where the baryonic contribution becomes negligible and the curvature-induced component $v_{\text{cve}}(r)$ dominates, substituting Equation (14) into Equation (19) yields:

$$^{(3)}R = \frac{4(1+\varepsilon)}{c^2}\frac{v_{\text{cve}}^2(r)}{r^2} \tag{20}$$

and replacing $v_{\text{cve}}^2(r)$ from Equation (13) gives:

$$^{(3)}R = \frac{4(1+\varepsilon)}{c^2}\frac{V_0^2}{r^2}\left(\frac{r}{R_{\text{ref}}}\right)^{\varepsilon} \tag{21}$$

Equation (21) shows that the spatial curvature associated with the outer galactic region varies as $^{(3)}R \propto r^{\varepsilon-2}$, exactly mirroring the effective-density law of Equation (16).

For $\varepsilon = 0$ the curvature scales as r^{-2}, reproducing the constant-velocity regime; for $\varepsilon > 0$ and $\varepsilon < 0$ the curvature respectively strengthens or weakens with radius, in full consistency with the behavior of the fitted velocity profiles.

These relations establish a direct, quantitative link between the observed kinematics and the intrinsic geometry of space within the 4DEU theoretical framework. The effective density and the associated spatial curvature inferred from the rotation curves thus represent purely geometric quantities, not additional mass components. This provides the theoretical foundation for the statistical analysis presented in the following section, where the model parameters V_0 and ε of Equation (12) are derived from the observed galaxy rotation curves.

5. Methods

5.1. Dataset and Definition of the Fitting Domain

For the statistical analysis and model fitting, we use the SPARC database of galaxy rotation curves [2] [3] which provides homogeneous photometric and kinematic data for 176 nearby disk galaxies spanning a broad range of morphologies and luminosities. From SPARC we select galaxies for which 1) both the total observed curve $v_{\text{obs}}(r)$ and the baryonic contributions $v_{\text{bulge}}, v_{\text{disk}}, v_{\text{gas}}$ are available; 2) at least five data points survive quality cuts defined below; and 3) there exists a contiguous radial range in which the extra component dominates.

The latter condition is expressed as

$$v_{\text{extra}}(r) > 0.5 v_{\text{obs}}(r) \tag{22}$$

The threshold above is an operational criterion used to delimit the radial range where the extra component becomes clearly measurable and non-negligible within the observed rotation curve.

In velocity-squared terms, this condition implies:

$$\frac{v_{\text{extra}}^2}{v_{\text{obs}}^2} > 0.25$$

indicating that the curvature-induced contribution represents at least one quarter of the total dynamical support.

This threshold (0.5) was selected on the basis of a statistical analysis of the fitting stability performed by comparing a stricter dominance limit

$$\frac{v_{\text{extra}}^2}{v_{\text{obs}}^2} > 0.5 \Rightarrow v_{\text{extra}} > 0.707 v_{\text{obs}}$$

and a looser one

$$\frac{v_{\text{extra}}^2}{v_{\text{obs}}^2} > 0.0025 \Rightarrow v_{\text{extra}} > 0.05 v_{\text{obs}}$$

As summarized in Section 5.1.1, the lower threshold includes inner radii still influenced by baryonic dynamics, whereas the higher one yields a purer but much smaller and statistically less stable sample. The adopted value of ($v_{\text{extra}}/v_{\text{obs}} > 0.5$) therefore represents a balanced, operational compromise between physical representativeness and sample completeness.

Based on this criterion, the corresponding radial interval used for the fit is determined as follows.

The fitting interval is defined by Equation (22), retaining only the largest contiguous subset of data points that satisfy this condition. The procedure identifies the first radius at which the extra velocity exceeds half of the observed velocity, as specified by Equation (22), and includes all subsequent points for which the same condition remains continuously satisfied up to the outermost radius. If the condition is violated at any larger radius, the search restarts from the next point where it becomes valid again, ensuring that each selected interval corresponds to a fully contiguous domain fulfilling the adopted fitting criterion.

Operationally, the valid radial interval $[r_{\min}, r_{\max}]$ is determined through the as follows:

Starting from the innermost radius, the algorithm identifies the first index j such that the fitting condition $v_{\text{extra}} \geq 0.5 v_{\text{obs}}$ is satisfied for all subsequent data points without further violations.

If a violation is encountered at any larger radius, the algorithm restarts the search from the next radius where the fitting condition becomes valid again; that radius then defines the new $r_{\min}$. The corresponding limits are then defined as

$$r_{\min} = r_j \qquad r_{\max} = r_{\text{last}}$$

and the number of fitted points is:

$$N = (\text{last} - j + 1)$$

The index j identifies the position, within the ordered radial dataset, of the first radius from which the fitting condition remains continuously satisfied up to the outermost data point, thus defining the lower boundary $r_{\min}$ of the fitting domain.

Galaxies with $N < 5$ were excluded from the analysis.

All the per-galaxy tables used to generate the figures are provided in the accompanying Excel workbook [26], with one worksheet per galaxy.

Statistical Validation of the Adopted Threshold (0.5)

To determine the most appropriate dominance threshold for defining the fitting domain, the complete 4DEU fitting procedure was repeated for three different limits of the extra component: $v_{\text{extra}}/v_{\text{obs}} \geq 0.05$, 0.5, and 0.707 using the intermediate case (0.5) as a neutral reference for comparison.

This value was not assumed a priori but simply provides a symmetric midpoint between the two extremes—one too loose and one too strict—allowing the sensitivity of the fitted parameters to be quantified in both directions.

This test was designed to assess how the fitted parameters (V_0, ε) and their statistical properties depend on the chosen threshold.

For each galaxy, the parameters were derived through weighted least-squares regression in logarithmic space.

The results obtained at each threshold were compared using a reference subsample consisting of the 96 galaxies from the **0.707 case**, which are also included in the other two thresholds (129 at 0.5, shown in **Table 1**, and 141 at 0.05).

Full fitting results for the 0.05 and 0.707 cases are available as supplementary Excel files at https://doi.org/10.5281/zenodo.17559295 providing a consistent basis for cross-threshold comparison.

The logarithmic slope ε—which quantifies the radial flexibility of the curvature-induced extra component—remains within one standard deviation of the 0.5-reference value for 100% of the galaxies at the 0.05 threshold and 84% at 0.707, demonstrating the robustness of the fitted shape. The amplitude V_0 remains within one standard deviation for 77% (0.05) and 39% (0.707) of the galaxies.

Excessively loose or restrictive thresholds thus tend to increase the degeneracy between V_0 and ε.

The mean **Pearson correlation coefficient** between the fitted parameters V_0 and ε quantifies their statistical dependence within the logarithmic regression. Its negative sign reflects the natural trade-off between slope and normalization in a power-law fit: a steeper ε can be partially compensated by a lower V_0, and vice versa.

The mean values obtained across the three thresholds are

$$\rho(0.05) \simeq -0.20;\ \rho(0.5) \simeq -0.24;\ \rho(0.707) \simeq -0.46$$

According to the conventional interpretation proposed by Cohen (Chapter 3 in [27]), coefficients with $|\rho| \lesssim 0.3$ indicate weak or negligible dependence between parameters, whereas values exceeding $|\rho| \gtrsim 0.5$ denote strong coupling and possible degeneracy. In this context, the correlations measured at 0.05 and 0.5 correspond to weak parameter dependence, while the value obtained at 0.707 indicates a moderate coupling caused by the reduced radial range of the fit.

The weighted-mean parameters obtained across the full 96-galaxy sample are:

$$\langle \varepsilon \rangle = 0.64 \pm 0.02 \qquad \langle V_0 \rangle = 46.3 \pm 1.2 \text{ km} \cdot \text{s}^{-1}$$

with an average goodness-of-fit probability $\langle p_{\text{gof}} \rangle \simeq 0.93$.

These averages differ by less than 2% among the three thresholds, confirming the overall stability of the 4DEU fits.

On the basis of this comparative analysis, the intermediate threshold $v_{\text{extra}}/v_{\text{obs}} \geq 0.5$ was selected as the adopted operational criterion. It represents a balanced and physically meaningful compromise between 1) the purity of the curvature-dominated regime, 2) the statistical independence of the fitted parameters, and 3) the retention of a sufficiently large number of galaxies for reliable parameter estimation.

5.2. Extra Component (Definition and Physical Meaning)

At each radius we define

$$v_{\text{extra}}^2(r) = v_{\text{obs}}^2(r) - v_{\text{bar}}^2(r) \tag{23}$$

where

$$v_{\text{bar}}^2 = v_{\text{bulge}}^2 + v_{\text{disk}}^2 + v_{\text{gas}}^2 \tag{24}$$

In the 4DEU framework this "extra" term is not an additional mass component; it represents the geometric contribution of 3D spatial curvature generated by the gravitational constraint that locally blocks the 3D-only expansion within bound systems.

5.3. Uncertainties

SPARC provides uncertainties only on v_{obs}, while errors on the baryonic terms are not tabulated. The dominant source of uncertainty arises from the estimate of baryonic contributions, which depends on the adopted mass-to-light ratio (M/L). Several studies ([2] [28]) show that the typical uncertainty on M/L is on the order of 20% - 30%.

To incorporate this physical variability, a conservative value of ±25% is applied to each baryonic component. The full propagation of uncertainties is explicitly derived below [29].

The baryonic velocity contribution is computed as the quadratic sum of the bulge, disk, and gas components (see Equation (24)), each affected by a systematic uncertainty of ±25% on the velocity amplitude. The corresponding propagated uncertainty on the baryonic term is given by:

$$\sigma_{v_{\text{bar}}} = \frac{1}{v_{\text{bar}}} \sqrt{\left(v_{\text{bulge}}\sigma_{v_{\text{bulge}}}\right)^2 + \left(v_{\text{disk}}\sigma_{v_{\text{disk}}}\right)^2 + \left(v_{\text{gas}}\sigma_{v_{\text{gas}}}\right)^2} \tag{25}$$

where $\sigma_{v_{\text{bulge}}} = 0.25 v_{\text{bulge}}$, $\sigma_{v_{\text{disk}}} = 0.25 v_{\text{disk}}$ and $\sigma_{v_{\text{gas}}} = 0.25 v_{\text{gas}}$.

The propagated uncertainty on the extra velocity component (v_{extra}), is then:

$$\sigma_{v_{\text{extra}}} = \frac{1}{v_{\text{extra}}} \sqrt{\left(v_{\text{obs}}\sigma_{v_{\text{obs}}}\right)^2 + \left(v_{\text{bar}}\sigma_{v_{\text{bar}}}\right)^2} \tag{26}$$

Points for which $v_{\text{extra}} \le 0$ or non-finite propagated uncertainties $\sigma_{v_{\text{extra}}}$ occur are automatically excluded from the fit, since the error-propagation formula contains terms proportional to $v_{\text{obs}}/v_{\text{extra}}$, which diverge when $v_{\text{obs}}^2 \approx v_{\text{bar}}^2$. This condition ensures numerical stability and prevents spurious weights in the logarithmic regression.

In logarithmic space, the corresponding uncertainty becomes:

$$\sigma_{\ln v_{\text{extra}}} = \frac{\sigma_{v_{\text{extra}}}}{v_{\text{extra}}} \tag{27}$$

Points yielding non-finite or numerically vanishing uncertainties $\sigma_{\ln v_{\text{extra}}}$ (typically arising when $v_{\text{obs}}^2 \approx v_{\text{bar}}^2$) are automatically excluded to prevent numerical instabilities and spurious overweighting in the logarithmic regression.

The statistical weights adopted in the **Weighted Least-Squares** (WLS) regression are:

$$w_i = \frac{1}{\sigma_{\ln v_{\text{extra}},i}^2} \tag{28}$$

where the subscript $i = 1, 2, \cdots, N_{\text{fit}}$ labels the individual data points included in the fit, each corresponding to an observed radius r_i in the selected interval. N_{fit} denotes the number of valid points satisfying the fitting criterion defined in Equation (22).

This choice minimizes the risk of underestimating the real errors and ensures a more robust statistical evaluation of the fit.

5.4. Calculation of the Reference Radius (R_{ref})

To define a unique and representative reference radius within the analyzed interval, we adopt the **geometric mean** of the radii r_i effectively included in the fit, defined as

$$R_{\text{ref}} = \mathrm{e}^{\langle \ln r \rangle}$$

where $\langle \ln r \rangle$ is the arithmetic mean of the logarithms of the fitted radii.

Formally, for a set of N valid data points located at radii $r_1 = r_{\min}, r_2, \cdots, r_N = r_{\text{last}}$,

$$\langle \ln r \rangle = \frac{1}{N} \sum_{i=1}^{N} \ln r_i$$

and therefore

$$R_{\text{ref}} = \exp\left(\frac{1}{N} \sum_{i=1}^{N} \ln r_i \right) \tag{29}$$

This construction is equivalent to taking the geometric mean of the radii r_i and corresponds to the logarithmic barycenter of the fitted segment. It provides a representative spatial scale for the entire fitting interval—one that captures the central tendency of the data in logarithmic space and is not biased by the extreme values of the range.

Consequently, R_{ref} serves as an optimal normalization point for Equation

(12), ensuring that the parameter V_0 characterizes the overall amplitude of the extra component across the analyzed region rather than at a single edge of the rotation curve.

5.4.1. 4DEU Kinematic Law and Determination of the Model Parameters V_0 and ε

Within the 4DEU theoretical framework, the curvature-induced extra velocity component is described by the kinematic relation (Equation (12)):

$$v_{\mathrm{cve}}(r) = V_0 \left(\frac{r}{R_{\mathrm{ref}}} \right)^{\varepsilon/2}$$

where V_0 and ε are the only free parameters of the model.

V_0 represents the characteristic amplitude of the curvature-induced velocity at the reference radius R_{ref}, while ε quantifies the **local logarithmic slope** of the extra component within the fitted range. Positive values of ε correspond to mildly rising profiles, $\varepsilon = 0$ to perfectly flat curves, and $\varepsilon < 0$ to weakly declining behaviors approaching the baryonic-Newtonian regime.

Parameter estimation is performed through a **Weighted Least-Squares (WLS)** regression in logarithmic space, which linearizes Equation (12) into

$$\ln v_{\mathrm{cve}} = \ln V_0 + \frac{\varepsilon}{2} \ln \left(\frac{r}{R_{\mathrm{ref}}} \right) \tag{30}$$

Each data point is weighted by the inverse variance of $\ln v_{\mathrm{extra}}$, with the corresponding logarithmic uncertainties propagated from the linear errors such as:

$$\sigma_{\ln v_{\mathrm{extra},i}} = \frac{\sigma_{v_{\mathrm{extra},i}}}{v_{\mathrm{extra},i}}$$

The fitting weights were based exclusively on the observational uncertainties of v_{extra}. The propagated uncertainties of the model velocity v_{cve}, derived from the fitted parameters V_0 and ε, were not included in the regression, since model errors depend on the fitted parameters themselves. This approach, commonly adopted in astrophysical and cosmological data analysis (e.g., [2] [28]), avoids introducing circular dependencies in the estimation of parameter uncertainties.

By construction, the logarithmic form of Equation (12) corresponds to a linear relation with slope $\beta = \varepsilon/2$.

Therefore, after the weighted least-squares regression the physical parameters are obtained as:

$$\varepsilon = 2\beta \qquad \sigma_\varepsilon = 2\sigma_\beta$$

where σ_β is the formal standard error of the fitted slope, and the factor of two simply reflects the linear relation $\varepsilon = 2\beta$ defined by Equation (12).

This convention corresponds to the operational procedure adopted in all 4DEU fits and ensures consistency between the kinematic formulation and the theoretical definition of ε.

5.4.2. Log-Log Formulation for Parameter Estimation

For each galaxy, the 4DEU kinematic relation is expressed in logarithmic form (see Equation (30)):

$$\ln v_{\mathrm{cve},i} = \ln V_0 + \frac{\varepsilon}{2}\ln\left(\frac{r_i}{R_{\mathrm{ref}}}\right)$$

This equation can be recast in the linear model:

$$y_i = \alpha + \beta x_i$$

so that the 4DEU relation model (Equation (12)):

$$v(r) = V_0\left(\frac{r}{R_{\mathrm{ref}}}\right)^{\varepsilon/2}$$

where:

$$y_i = \ln v_{\mathrm{extra},i},\ x_i = \ln\left(\frac{r_i}{R_{\mathrm{ref}}}\right),\ \alpha = \ln V_0,\ \beta = \varepsilon/2$$

From the fitted coefficients one obtains

$$V_0 = \mathrm{e}^{\alpha} \qquad \varepsilon = 2\beta$$

and the corresponding standard errors

$$\sigma_{V_0} = V_0\sigma_\alpha \qquad \sigma_\varepsilon = 2\sigma_\beta$$

This formulation ensures that the fitted slope β directly represents half the logarithmic gradient of the extra velocity, while V_0 is its normalization at the reference radius R_{ref}.

The observational values $y_i = \ln v_{\mathrm{extra}}(r_i)$ are compared with the theoretical law $y_{\mathrm{model}} = \alpha + \beta x_i$, which represents the logarithmic form of the 4DEU model.

5.4.3. Weighted Least-Squares Estimation

The slope β and intercept α are obtained by minimizing the weighted residuals, leading to the classical WLS estimators [29] [30]:

$$\beta = \frac{SS_{xy} - S_x S_y}{\Delta},\ \alpha = \frac{S_{xx}S_y - S_x S_{xy}}{\Delta}$$

where $S = \sum w_i$, $S_x = \sum w_i x_i$, $S_y = \sum w_i y_i$, $S_{xx} = \sum w_i x_i^2$, $S_{xy} = \sum w_i x_i y_i$ and $\Delta = SS_{xx} - S_x^2$.

The statistical weights are defined as:

$$w_i = \frac{1}{\sigma_{y,i}^2}$$

With $\sigma_{y,i} \equiv \sigma_{\ln v_{\mathrm{extra},i}} = \dfrac{\sigma_{v_{\mathrm{extra},i}}}{v_{\mathrm{extra},i}}$

From the fitted parameters:

$$V_0 = \mathrm{e}^{\alpha},\quad \varepsilon = 2\beta$$

The standard deviations of the fitted parameters are given by the WLS relations:

$$\sigma_\beta = \sqrt{\frac{S}{\Delta}}, \quad \sigma_\alpha = \sqrt{\frac{S_{xx}}{\Delta}}$$

and their propagated uncertainties:

$$\sigma_\varepsilon = 2\sigma_\beta$$

5.5. Statistical Test

All statistical evaluations are performed in logarithmic space, so that the residuals are computed on $\ln v_{\text{extra}}$ rather than on the velocities themselves. This is statistically consistent with the weighted log-log regression adopted for the power-law model.

5.5.1. Goodness-of-Fit Metrics

The global agreement between the model and the data is quantified through the chi-squared statistic:

$$\chi^2 = \sum_{i=1}^{N} \frac{\left[\ln v_{\text{extra},i} - \ln v_{\text{cve},i}\right]^2}{\sigma^2_{\ln v_{\text{extra},i}}}$$

where $v_{\text{extra},i}$ are the empirical extra velocities derived from observations, $v_{\text{cve},i}$ are the model values given by Equation (12), and $\sigma_{\ln v_{\text{extra},i}} = \dfrac{\sigma_{v_{\text{extra},i}}}{v_{\text{extra},i}}$ are the propagated logarithmic uncertainties defined in Equation (27) (with $\sigma_{v_{\text{extra},i}}$ given by Equation (26)).

The **degrees of freedom** are defined as:

$$\nu = N - k \tag{31}$$

where $k = 2$ because both parameters V_0 and ε are always treated as free quantities obtained directly from the fit.

The corresponding goodness-of-fit probability is computed as:

$$p_{\text{gof}} = 1 - F_{\chi^2}\left(\chi^2; \nu\right) \tag{32}$$

where F_{χ^2} is the cumulative distribution function of the chi-squared distribution with ν degrees of freedom.

Fitting is considered **statistically consistent** when

$$p_{\text{gof}} \geq 0.01$$

corresponding to a 99% confidence threshold below which the model would be rejected.

5.5.2. Method Adopted for Constructing the Observed-Model Velocity Plots

For each galaxy, two complementary graphical comparisons are produced to illustrate the agreement between the observed and modeled quantities.

Extra component:

The first comparison is performed between the observed extra velocity (derived from Equation (23),

$$v_{\text{extra}}(r)=\sqrt{v_{\text{obs}}^2(r)-v_{\text{bar}}^2(r)} \tag{33}$$

and the corresponding 4DEU prediction,

$$v_{\text{cve}}(r)=V_0\left(\frac{r}{R_{\text{ref}}}\right)^{\varepsilon/2}$$

This comparison quantifies how accurately the curvature-induced term of Equation (12) reproduces the extra component derived from the data.

Total rotation curve:

The second comparison is carried out between the total velocity reconstructed from the model,

$$v_{\text{mod}}(r)=\sqrt{v_{\text{cve}}^2(r)+v_{\text{bar}}^2(r)} \tag{34}$$

and the observed total rotation curve $v_{\text{obs}}(r)$.

This representation allows a direct visual comparison between the total modeled velocity—obtained by combining in quadrature the baryonic and curvature-induced components—and the observed rotation curve, in order to evaluate the overall agreement between data and model.

Depending on the relative separation between the two pairs of curves $(v_{\text{obs}}, v_{\text{mod}})$ and $(v_{\text{extra}}, v_{\text{cve}})$, the graphs are displayed either with a dual y-axis layout—using different scales to enhance visibility—or, when the two pairs are well distinguished, with a single y-axis for clearer visual continuity. This flexible representation allows the trends of both comparisons to be appreciated simultaneously, providing a compact and physically transparent view of the model-data consistency for each galaxy.

6. Results

This section summarizes the numerical and statistical results obtained by applying the 4DEU model to the SPARC galaxy sample.

6.1. Analyzed Sample

The SPARC database contains 176 disk galaxies with well-resolved rotation curves and detailed baryonic decompositions [2] [3]. Among these, **129 systems** satisfy the quality and physical selection criteria described in Section 5 namely:

- both the total observed velocity $v_{\text{obs}}(r)$ and all baryonic components ($v_{\text{bulge}}, v_{\text{disk}}, v_{\text{gas}}$) are tabulated;
- at least five data points survive the quality cuts, and
- a contiguous radial interval exists where the extra velocity component clearly dominates, fulfilling the operational condition (Equation (22)), ensuring that the fit is performed entirely within the domain dominated by the extra velocity component.

The results for each galaxy—fitted parameters V_0 and ε, their uncertainties, the χ^2 statistic, the degrees of freedom ν, the goodness-of-fit probability

p_{gof}, and the statistical classification—are listed in Table 1. Out of the 129 analyzed galaxies, **128 yield statistically consistent fits** with $p_{\text{gof}} \geq 0.01$, while **only one galaxy (UGC 05764) falls below this threshold** and is classified as **not consistent** (see Table 1).

Table 1. Best-fit 4DEU parameters and goodness-of-fit statistics for the 129 SPARC galaxies analyzed.

Galaxy	N	R_{min} (kpc)	R_{max} (kpc)	R_{ref} (kpc)	ε	σ_{ε}	$\Delta\chi^2$	Model	V_0 (Km/s)	σ_{V_0}	χ^2	p_{gof}	Model fitting
D564-8	6	0.51	3.07	1.5287	1.2422	0.3579	12.0487	$\varepsilon > 0$	15.343	1.3921	0.8962	0.9251	Consistent
D631-7	12	2.25	7.19	4.4398	1.2603	0.2146	34.5040	$\varepsilon > 0$	43.837	1.3086	5.2252	0.8756	Consistent
DDO064	14	0.1	2.98	1.0499	1.2448	0.2839	19.2204	$\varepsilon > 0$	24.377	2.2411	3.0970	0.9948	Consistent
DDO154	11	0.99	5.92	3.0379	0.7764	0.0876	78.5486	$\varepsilon > 0$	36.234	0.6936	15.2422	0.0845	Consistent
DDO161	21	3.9	13.37	8.1217	0.9459	0.1704	30.8155	$\varepsilon > 0$	47.900	1.4362	2.9985	1.0000	Consistent
DDO168	8	1.24	4.12	2.4964	0.9467	0.3093	9.3670	$\varepsilon > 0$	39.581	1.8289	6.7938	0.3403	Consistent
DDO170	8	1.87	12.33	6.0926	0.6527	0.1411	21.4036	$\varepsilon > 0$	43.901	1.5769	3.4622	0.7490	Consistent
ESO079-G014	10	4.39	16.67	9.0149	0.7637	0.5611	1.8526	$\varepsilon > 0$	96.128	11.2124	0.5061	0.9999	Consistent
ESO116-G012	11	2.68	9.86	5.5628	0.7582	0.2839	7.1347	$\varepsilon > 0$	78.863	4.5740	1.1511	0.9990	Consistent
ESO444-G084	7	0.26	4.44	1.4902	0.9266	0.0933	98.5891	$\varepsilon > 0$	41.397	1.4253	3.7702	0.5830	Consistent
ESO563-G021	14	20.3	42.41	30.5761	1.3011	0.9376	1.9257	$\varepsilon > 0$	203.552	22.6649	0.2233	1.0000	Consistent
F563-1	17	1.07	20.1	6.7856	0.4631	0.1030	20.2214	$\varepsilon > 0$	83.883	3.4605	8.0100	0.9234	Consistent
F563-V2	10	0.28	10.47	3.0020	0.8374	0.1750	22.8974	$\varepsilon > 0$	74.611	5.1944	6.9688	0.5400	Consistent
F565-V2	7	1.26	8.8	4.2512	1.0167	0.3011	11.3990	$\varepsilon > 0$	54.137	4.3324	1.2722	0.9378	Consistent
F568-1	12	0.44	13.23	4.2248	0.7617	0.1725	19.5038	$\varepsilon > 0$	87.806	5.0339	5.0603	0.8871	Consistent
F568-3	16	1.8	17.98	5.8058	0.7440	0.1697	19.2192	$\varepsilon > 0$	66.731	3.7707	5.2365	0.9822	Consistent
F568-V1	15	0.39	17.63	4.5703	0.4081	0.1479	7.6143	$\varepsilon > 0$	89.842	3.5936	3.6625	0.9943	Consistent
F571-8	6	5.44	15.55	8.5346	0.7747	0.2914	7.0669	$\varepsilon > 0$	107.405	6.8079	1.3168	0.8585	Consistent
F571-V1	7	1.95	13.59	6.5703	0.7229	0.3380	4.5734	$\varepsilon > 0$	59.170	5.1735	0.9742	0.9646	Consistent
F574-1	14	0.47	12.6	4.9587	0.5608	0.1681	11.1264	$\varepsilon > 0$	67.240	3.4016	5.1008	0.9545	Consistent
F579-V1	14	0.42	15.16	4.7217	0.2867	0.1393	4.2380	$\varepsilon > 0$	79.901	4.8646	4.6192	0.9695	Consistent
F583-1	22	0.89	16.26	4.0599	0.8146	0.1023	63.3710	$\varepsilon > 0$	52.839	1.6128	17.8679	0.5961	Consistent
F583-4	12	0.22	7.29	2.8752	0.9727	0.2389	16.5743	$\varepsilon > 0$	35.087	3.3366	0.5412	1.0000	Consistent
IC2574	29	2.28	10.23	5.7492	1.5542	0.1588	95.8432	$\varepsilon > 0$	36.689	1.1485	3.6561	1.0000	Consistent
KK98-251	15	0.25	3.13	1.2046	1.6808	0.2893	33.7644	$\varepsilon > 0$	13.636	1.2880	2.6751	0.9989	Consistent
NGC0024	28	0.32	11.27	1.7457	0.4632	0.0676	46.9981	$\varepsilon > 0$	65.020	3.2972	4.2457	1.0000	Consistent
NGC0055	17	3.68	13.5	8.0165	0.7372	0.3128	5.5551	$\varepsilon > 0$	57.178	2.9642	1.6875	1.0000	Consistent
NGC0100	14	3.42	9.62	6.2768	1.1557	0.4103	7.9333	$\varepsilon > 0$	62.108	3.8082	0.1013	1.0000	Consistent
NGC0247	26	1.08	14.54	6.4469	0.7841	0.0949	68.2497	$\varepsilon > 0$	63.947	2.2376	3.6093	1.0000	Consistent
NGC0289	20	13.57	71.12	38.2394	0.1704	0.2239	0.5795	$\varepsilon > 0$	134.545	5.8181	4.7992	0.9991	Consistent
NGC0300	24	1.36	11.8	5.6608	0.7986	0.1575	25.6982	$\varepsilon > 0$	66.070	2.7419	3.3857	1.0000	Consistent

Continued

NGC1003	30	6.22	30.24	16.6410	0.6527	0.0909	51.5314	$\varepsilon > 0$	87.749	1.6969	5.3882	1.0000	Consistent
NGC1090	9	20.13	30.09	24.9004	0.8958	1.9847	0.2037	$\varepsilon > 0$	100.736	12.7844	0.0282	1.0000	Consistent
NGC1705	14	0.22	6	2.3424	0.2804	0.1297	4.6781	$\varepsilon > 0$	61.242	2.1740	0.8769	1.0000	Consistent
NGC2366	20	1.54	6.06	3.5311	0.6576	0.2190	9.0146	$\varepsilon > 0$	38.573	1.2480	6.3352	0.9946	Consistent
NGC2403	33	4.97	20.87	11.9591	0.5793	0.1291	20.1452	$\varepsilon > 0$	104.537	2.4589	1.1315	1.0000	Consistent
NGC2683	6	17.31	34.62	25.1958	0.1658	1.1532	0.0207	$\varepsilon > 0$	109.060	15.9143	0.3437	0.9868	Consistent
NGC2841	26	12.31	63.64	34.3856	0.4287	0.1209	12.5848	$\varepsilon > 0$	224.697	5.9153	2.4094	1.0000	Consistent
NGC2903	11	15.36	24.96	19.9280	0.8486	1.4102	0.3621	$\varepsilon > 0$	118.968	12.6634	0.0783	1.0000	Consistent
NGC2915	26	1.68	10.04	5.2307	0.1623	0.1046	2.4048	$\varepsilon > 0$	75.988	1.7485	5.1526	1.0000	Consistent
NGC2998	5	22.46	42.28	31.5807	0.6817	1.5789	0.1864	$\varepsilon > 0$	132.792	22.6632	0.0753	0.9946	Consistent
NGC3109	25	0.26	6.45	2.6263	1.4460	0.0558	671.0939	$\varepsilon > 0$	35.852	0.6907	13.9941	0.9270	Consistent
NGC3198	19	10.04	44.08	23.8185	0.4140	0.2135	3.7607	$\varepsilon > 0$	112.882	5.3261	0.3711	1.0000	Consistent
NGC3741	20	0.47	7	2.5164	0.8886	0.0664	179.2097	$\varepsilon > 0$	33.101	0.7136	5.8817	0.9967	Consistent
NGC3769	8	8.72	37.16	18.0764	0.4834	0.3320	2.1205	$\varepsilon > 0$	87.140	8.5476	0.4621	0.9983	Consistent
NGC3917	15	2.61	14.86	7.7783	0.6762	0.3698	3.3432	$\varepsilon > 0$	77.341	7.9844	0.5881	1.0000	Consistent
NGC3992	5	27.52	46.02	36.1630	0.6907	1.5804	0.1910	$\varepsilon > 0$	163.464	23.7362	0.0466	0.9974	Consistent
NGC4010	5	6.98	10.47	8.6356	0.0143	2.6628	0.0000	$\varepsilon > 0$	74.273	14.4314	0.0027	1.0000	Consistent
NGC4013	18	18.58	31.01	24.5191	1.3578	0.7809	3.0231	$\varepsilon > 0$	122.094	7.0614	0.9591	1.0000	Consistent
NGC4100	14	11.35	22.76	16.6567	0.1558	1.1203	0.0193	$\varepsilon > 0$	107.608	12.2077	0.3454	1.0000	Consistent
NGC4157	5	22.65	29.61	26.0135	1.6365	3.7055	0.1950	$\varepsilon > 0$	116.145	20.1854	0.0084	0.9998	Consistent
NGC4183	23	0.87	21.02	8.3019	0.5310	0.1562	11.5517	$\varepsilon > 0$	71.924	3.9851	0.9771	1.0000	Consistent
NGC4214	11	1.46	5.63	3.2761	0.5388	0.3380	2.5408	$\varepsilon > 0$	65.676	3.5831	0.5852	0.9999	Consistent
NGC4559	16	11.13	20.97	15.7406	0.4773	0.7595	0.3950	$\varepsilon > 0$	82.298	5.6026	0.2885	1.0000	Consistent
NGC5033	14	14.91	44.59	28.1670	0.1492	0.3188	0.2191	$\varepsilon > 0$	149.964	7.6258	1.1904	1.0000	Consistent
NGC5055	10	28.74	54.59	40.8391	0.7340	1.1294	0.4224	$\varepsilon > 0$	117.171	12.9216	0.1315	1.0000	Consistent
NGC5585	12	3.42	10.96	6.7696	0.6222	0.3185	3.8155	$\varepsilon > 0$	68.235	3.5594	2.1800	0.9948	Consistent
NGC5907	10	27.68	50.33	38.3190	1.0174	1.0225	0.9901	$\varepsilon > 0$	142.968	14.1762	0.1545	1.0000	Consistent
NGC5985	33	3.54	34.72	13.8197	0.1247	0.1152	1.1711	$\varepsilon > 0$	200.356	8.2134	3.2413	1.0000	Consistent
NGC6015	23	11.13	29.23	19.4087	0.3761	0.2744	1.8784	$\varepsilon > 0$	122.994	4.5361	3.4902	1.0000	Consistent
NGC6503	24	6.07	23.5	13.7719	0.4572	0.1921	5.6638	$\varepsilon > 0$	90.871	3.0706	0.7328	1.0000	Consistent
NGC6674	14	7.49	72.41	33.5424	0.4796	0.2551	3.5350	$\varepsilon > 0$	172.449	13.7236	0.7306	1.0000	Consistent
NGC6946	7	18.24	20.4	19.2867	0.3635	12.7485	0.0008	$\varepsilon > 0$	86.381	20.2331	0.0091	1.0000	Consistent
NGC7331	7	29.89	36.31	33.0642	2.2379	5.4211	0.1704	$\varepsilon > 0$	137.269	24.5153	0.0144	1.0000	Consistent
NGC7793	12	3.68	7.87	5.1817	−0.3165	1.1553	0.0750	$\boldsymbol{\varepsilon < 0}$	62.493	9.1977	0.2435	1.0000	Consistent
NGC7814	10	9.5	19.53	14.1669	0.9222	0.6695	1.8975	$\varepsilon > 0$	145.857	11.2142	0.0164	1.0000	Consistent
UGC00128	22	1.25	53.75	20.5595	0.3055	0.0492	38.5300	$\varepsilon > 0$	106.326	1.7486	7.3330	0.9954	Consistent
UGC00191	9	0.62	9.98	2.1859	0.6486	0.1226	28.0022	$\varepsilon > 0$	43.879	3.1573	4.9296	0.6686	Consistent

Continued

UGC00731	12	0.91	10.91	4.8081	0.6100	0.0648	88.7405	$\varepsilon > 0$	55.765	1.1440	8.1328	0.6159	Consistent
UGC00891	5	1.48	7.39	3.8616	1.1260	0.2310	23.7621	$\varepsilon > 0$	40.765	2.4475	1.1835	0.7570	Consistent
UGC01230	10	2.35	36.54	10.6115	0.1011	0.1413	0.5113	$\varepsilon > 0$	85.673	5.1046	3.0628	0.9304	Consistent
UGC01281	23	0.38	4.99	1.8342	1.2951	0.1923	45.3752	$\varepsilon > 0$	29.301	1.9286	6.8971	0.9983	Consistent
UGC02259	8	1.02	8.14	3.8333	0.4041	0.0944	18.3104	$\varepsilon > 0$	67.723	2.0747	0.6193	0.9961	Consistent
UGC02487	13	20.09	80.38	46.3254	0.2621	0.2687	0.9514	$\varepsilon > 0$	260.136	13.5373	0.6547	1.0000	Consistent
UGC02885	12	31.22	74.07	50.8219	0.9795	0.6149	2.5375	$\varepsilon > 0$	199.695	16.1760	0.2235	1.0000	Consistent
UGC02916	7	19.05	38	27.7994	−0.3311	1.2053	0.0755	$\boldsymbol{\varepsilon < 0}$	113.135	15.6193	0.1356	0.9997	Consistent
UGC02953	33	20.43	62.39	37.9878	0.6580	0.2389	7.5830	$\varepsilon > 0$	193.783	7.5648	0.4124	1.0000	Consistent
UGC03205	14	15.71	40.04	22.1973	1.0653	0.4284	6.1832	$\varepsilon > 0$	134.832	13.0710	0.1823	1.0000	Consistent
UGC03546	5	19.45	29.23	23.2682	1.4999	1.8654	0.6466	$\varepsilon > 0$	123.019	17.3444	0.0026	1.0000	Consistent
UGC03580	15	8.58	27.06	13.7049	0.7726	0.1855	17.3525	$\varepsilon > 0$	89.462	3.9886	5.0367	0.9744	Consistent
UGC04278	25	0.14	6.69	2.5832	1.6420	0.2039	64.8803	$\varepsilon > 0$	37.849	2.6479	4.7068	1.0000	Consistent
UGC04325	8	0.7	5.59	2.6293	0.5601	0.1301	18.5345	$\varepsilon > 0$	66.433	2.7003	8.2944	0.2173	Consistent
UGC04483	6	0.4	1.21	0.7570	0.7709	0.4144	3.4609	$\varepsilon > 0$	16.673	1.2419	0.3932	0.9830	Consistent
UGC04499	8	1.82	8.18	4.5050	0.7605	0.3373	5.0821	$\varepsilon > 0$	48.438	3.4393	0.5929	0.9965	Consistent
UGC05005	9	3.91	28.61	11.3958	0.9811	0.3549	7.6426	$\varepsilon > 0$	61.686	7.4243	1.3096	0.9882	Consistent
UGC05253	14	16.61	53.29	30.6419	0.2184	0.3000	0.5298	$\varepsilon > 0$	157.815	9.6940	0.9648	1.0000	Consistent
UGC05716	12	1.03	12.37	5.4610	0.5266	0.0780	45.5901	$\varepsilon > 0$	56.487	1.1579	5.3391	0.8674	Consistent
UGC05721	22	0.27	6.74	2.0606	0.1838	0.0903	4.1452	$\varepsilon > 0$	67.008	2.3151	10.9907	0.9465	Consistent
UGC05750	9	2.52	22.85	6.5190	0.8002	0.3022	7.0122	$\varepsilon > 0$	44.716	3.8901	1.5186	0.9817	Consistent
UGC05764	10	0.36	3.62	1.6412	0.6430	0.0662	94.4375	$\varepsilon > 0$	43.889	0.6274	35.8709	1.9E−05	Not Consistent
UGC05829	11	0.63	6.91	3.0862	1.0372	0.2219	21.8545	$\varepsilon > 0$	36.090	2.2941	0.4279	1.0000	Consistent
UGC05918	8	0.56	4.46	2.0979	0.7066	0.2183	10.4802	$\varepsilon > 0$	30.226	1.8183	1.0991	0.9816	Consistent
UGC05986	13	1.88	9.41	5.0873	0.5989	0.2600	5.3050	$\varepsilon > 0$	82.842	4.6029	2.9871	0.9909	Consistent
UGC06399	9	0.87	7.85	3.6172	0.9232	0.2937	9.8828	$\varepsilon > 0$	53.210	4.2794	1.1965	0.9910	Consistent
UGC06446	17	0.58	10.22	4.1969	0.4694	0.1020	21.1622	$\varepsilon > 0$	63.858	1.7357	3.5900	0.9988	Consistent
UGC06614	6	24.94	64.59	37.0468	0.5690	0.5066	1.2613	$\varepsilon > 0$	149.883	13.2721	0.3104	0.9891	Consistent
UGC06667	9	0.87	7.85	3.6172	0.8262	0.0840	96.7844	$\varepsilon > 0$	62.126	1.3961	10.0084	0.1881	Consistent
UGC06786	16	8.52	34.05	17.9589	0.3439	0.1877	3.3558	$\varepsilon > 0$	172.772	7.2212	1.6308	1.0000	Consistent
UGC06787	26	8.98	37.19	18.8906	0.7197	0.1400	26.4132	$\varepsilon > 0$	180.548	5.9036	3.6576	1.0000	Consistent
UGC06917	10	2.61	10.47	6.0090	0.7177	0.3932	3.3314	$\varepsilon > 0$	71.159	5.3669	0.4096	0.9999	Consistent
UGC06930	9	3.5	16.61	9.2937	0.4347	0.3086	1.9849	$\varepsilon > 0$	74.566	5.5283	0.0488	1.0000	Consistent
UGC06983	16	2.61	15.68	8.1266	0.3938	0.1791	4.8347	$\varepsilon > 0$	84.718	3.0435	1.1641	1.0000	Consistent
UGC07089	7	5.24	9.16	7.1092	1.6684	1.4388	1.3448	$\varepsilon > 0$	47.577	6.4140	0.1011	0.9998	Consistent
UGC07125	10	5.76	18.68	11.4772	0.4734	0.4560	1.0777	$\varepsilon > 0$	42.390	3.2461	0.4817	0.9999	Consistent
UGC07151	9	1.5	5.5	3.2341	0.5334	0.5331	1.0011	$\varepsilon > 0$	44.994	4.6526	0.0212	1.0000	Consistent

Continued

UGC07261	7	0.95	6.67	3.2178	0.5296	0.2669	3.9379	$\varepsilon > 0$	49.622	4.5970	0.3079	0.9975	Consistent
UGC07323	5	3.5	5.82	4.5804	1.3813	2.4579	0.3158	$\varepsilon > 0$	44.612	9.8809	0.0234	0.9991	Consistent
UGC07399	10	0.61	6.13	2.7750	0.5836	0.1002	33.9114	$\varepsilon > 0$	78.666	2.0278	3.9603	0.8607	Consistent
UGC07524	30	0.69	10.69	4.6550	0.8172	0.1027	63.2680	$\varepsilon > 0$	50.591	1.4003	9.3352	0.9996	Consistent
UGC07559	5	1.08	2.53	1.7295	1.2073	1.3202	0.8363	$\varepsilon > 0$	19.353	3.2925	0.2790	0.9639	Consistent
UGC07603	10	1.02	4.11	2.3539	0.6419	0.2146	8.9447	$\varepsilon > 0$	49.019	2.0604	1.3013	0.9955	Consistent
UGC07608	8	0.6	4.78	2.2481	1.0770	0.2981	13.0568	$\varepsilon > 0$	43.281	3.3881	0.9490	0.9875	Consistent
UGC07690	6	1.18	4.13	2.4430	0.3023	0.7710	0.1537	$\varepsilon > 0$	37.420	5.8780	0.0195	1.0000	Consistent
UGC07866	7	0.33	2.32	1.1224	1.0573	0.6380	2.7469	$\varepsilon > 0$	16.502	3.0307	0.1153	0.9998	Consistent
UGC08286	17	0.47	8.04	3.3945	0.4924	0.0765	41.3864	$\varepsilon > 0$	62.339	1.5573	9.5525	0.8469	Consistent
UGC08490	30	0.34	10.15	4.0765	0.3003	0.0751	16.0068	$\varepsilon > 0$	64.830	1.5375	7.8638	0.9999	Consistent
UGC08550	11	0.49	5.36	2.3937	0.6426	0.1333	23.2563	$\varepsilon > 0$	41.498	1.5887	2.9218	0.9673	Consistent
UGC08699	9	10.21	25.7	16.6093	0.9864	0.5198	3.6017	$\varepsilon > 0$	125.111	9.9550	0.0926	1.0000	Consistent
UGC09037	6	19.46	25.51	22.4050	0.6192	4.9344	0.0157	$\varepsilon > 0$	83.679	18.5856	0.0134	1.0000	Consistent
UGC09133	27	27.66	108.31	59.9465	0.2689	0.1769	2.3108	$\varepsilon > 0$	177.150	5.7704	3.4450	1.0000	Consistent
UGC09992	5	0.78	3.89	2.0284	0.0430	0.9604	0.0020	$\varepsilon > 0$	18.495	5.5049	0.0151	0.9995	Consistent
UGC10310	7	1.1	7.74	3.7324	0.6500	0.2982	4.7505	$\varepsilon > 0$	47.099	3.8620	1.3547	0.9292	Consistent
UGC11820	10	0.26	15.82	2.3468	0.7192	0.0896	64.3911	$\varepsilon > 0$	37.807	2.6095	2.5975	0.9570	Consistent
UGC12506	31	0.82	49.99	18.9037	0.2082	0.0811	6.5893	$\varepsilon > 0$	170.766	6.3256	2.2965	1.0000	Consistent
UGC12632	15	0.71	10.66	4.5662	0.5619	0.1194	22.1391	$\varepsilon > 0$	50.774	1.6824	4.2982	0.9876	Consistent
UGC12732	16	0.96	15.4	6.5298	0.6750	0.0938	51.7770	$\varepsilon > 0$	63.349	1.7607	2.1156	0.9999	Consistent
UGCA281	7	0.09	1.08	0.4519	1.1491	0.3952	8.4554	$\varepsilon > 0$	13.915	1.9715	0.2429	0.9986	Consistent
UGCA442	8	0.42	6.33	2.5893	0.9522	0.0948	100.8552	$\varepsilon > 0$	35.825	1.3527	7.2346	0.2997	Consistent
UGCA444	36	0.12	2.62	1.0908	1.0615	0.1220	75.6921	$\varepsilon > 0$	21.116	0.8049	1.5415	1.0000	Consistent

6.2. General Trends of the Fitted Parameters

The overwhelming majority of galaxies exhibit **positive values of** ε, corresponding to **flat or mildly rising rotation curves** in their halo-dominated regions. This behavior reflects a **progressive increase of local 3D curvature** generated by the gravitational constraint that locally blocks the 3D-only cosmic expansion, leading to a slowly strengthening curvature-induced velocity component $v_{\mathrm{cve}}(r)$ with radius.

Only **two galaxies, NGC7793 (** $\varepsilon = -0.316 \pm 0.115$ **) and UGC02916 (** $\varepsilon = -0.331 \pm 0.121$ **), exhibit negative slopes**, indicating a weakly declining outer profile.

In these systems, the curvature-from-constraint contribution is partially weakened: the geometric support decreases gradually toward the baryonic-Newtonian regime. Both objects display extremely faint extra components in the SPARC data. For NGC7793, v_{extra} is numerically undefined (negative radicand) up to ≈ 2.5

kpc, and for UGC02916 up to ≈ 20 kpc, implying that the dynamics are purely baryonic within those radii.

Only beyond these limits does a small positive v_{extra} emerge, well reproduced by the fitted model with $\varepsilon < 0$.

Such weakly declining trends, illustrated in Figure 6, correspond to a gentle reduction of the *cve* support, consistent with mild warps, non-circular motions, or gas-pressure effects that lower the measured velocities without producing a Keplerian fall-off.

6.3. Representative Rotation-Curve Fits

Representative fits for the main morphological and kinematic categories are shown in Figures 2-7.

Each plot compares the observed rotation curve $v_{\text{obs}}(r)$, the baryonic contribution $v_{\text{bar}}(r)$, the curvature-induced component $v_{\text{cve}}(r)$ derived from Equation (12), and the total modeled velocity

$$v_{\text{mod}}(r) = \sqrt{v_{\text{bulge}}^2 + v_{\text{disk}}^2 + v_{\text{gas}}^2 + v_{\text{cve}}^2}$$

This total model curve represents the complete rotational velocity predicted by the 4DEU framework and is directly compared with the observations.

a) Large Bright Spirals—Benchmark cases (Figure 2). NGC2841 and NGC3198 display extended, well-measured rotation curves with excellent agreement between data and model. Both show slightly rising outer sections ($\varepsilon > 0$), typical of luminous Sc/Sb systems where the curvature-dominated regime emerges smoothly.

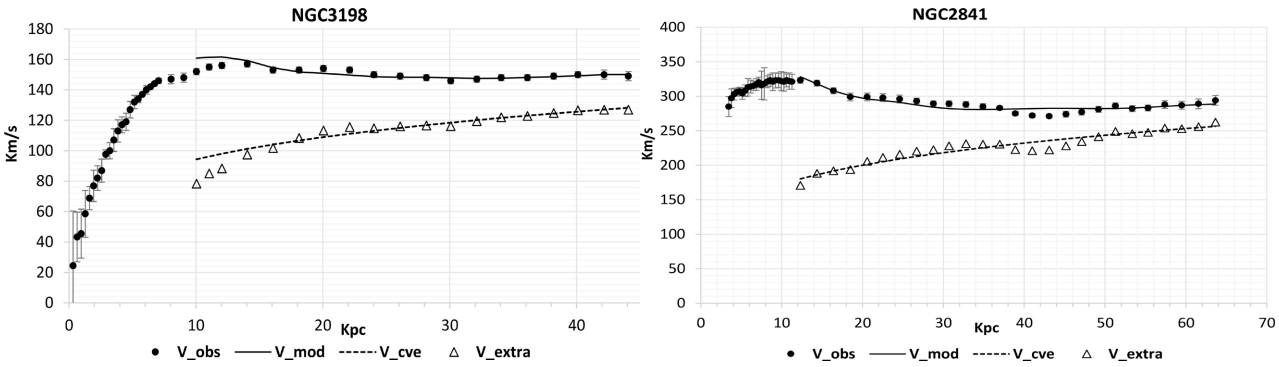

(a) (b)

Figure 2. 4DEU rotation-curve fits for large, bright spiral galaxies (Sc/Sb types). NGC2841 and NGC3198 exhibit extended, well-defined rotation curves with excellent agreement between data and model. Both display a mildly rising outer trend ($\varepsilon > 0$), consistent with classic, well-behaved Sc/Sb systems in which the **curvature-dominated regime** emerges smoothly at large radii. The fits reproduce the flat to slightly rising outer profiles without systematic residuals, making these galaxies representative benchmarks for bright spirals.

b) Intermediate and Compact Spirals (Figure 3). NGC 2403 and UGC08490 illustrate clean transitions from baryon-dominated inner radii to curvature-dominated outer disks. Their gently increasing profiles are reproduced with small pos-

itive ε, confirming the robustness of the model at intermediate masses.

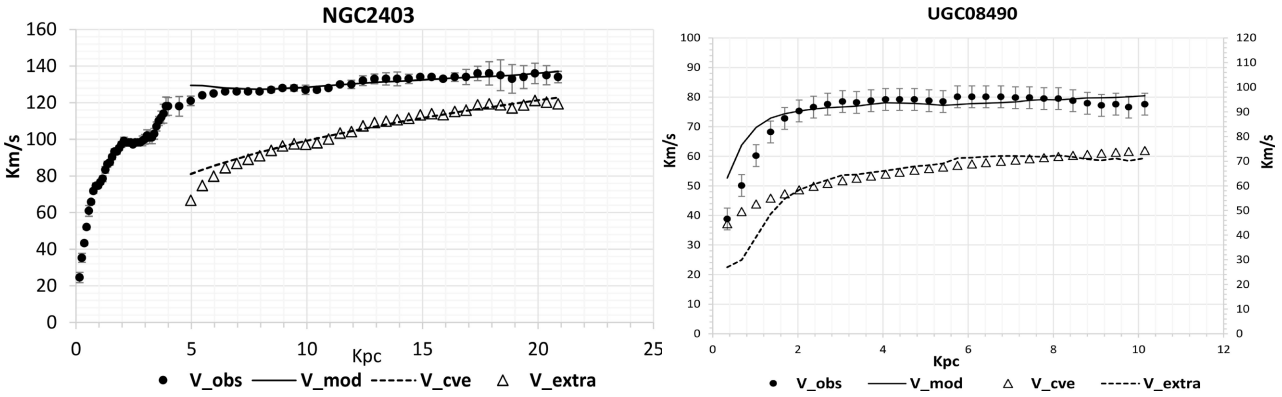

(a) (b)

Figure 3. 4DEU rotation-curve fits for intermediate and late-type spiral galaxies. NGC2403 shows a clear transition from a baryon-dominated inner region to a curvature-dominated outer disk, with a gentle outer rise well reproduced by the model ($\varepsilon > 0$). UGC08490, a compact late-type system, presents a smooth and low-scatter rotation curve over a shorter radial extent; despite its limited range, the fit accurately follows the gradual outer increase and the baryon/curvature crossover. Taken together, these two cases typify intermediate-mass spirals with regular kinematics and robust 4DEU fits.

Dwarf and Low-Surface-Brightness Galaxies (Figure 4). NGC 3741 is curvature-dominated at all radii, whereas UGCA444—a small, isolated ***dlrr*** galaxy—shows a more balanced inner disk. The pair brackets the typical behavior of low-mass systems, from extreme curvature control to modest halo dominance within the optical region.

Giant LSB Spirals (Figure 5). UGC 2885 and UGC 12506 extend to tens of kiloparsecs with diffuse stellar disks. The model reproduces their sustained outer speeds and the gradual strengthening of the curvature-induced component with radius, demonstrating the applicability of the 4DEU law at very large spatial scales.

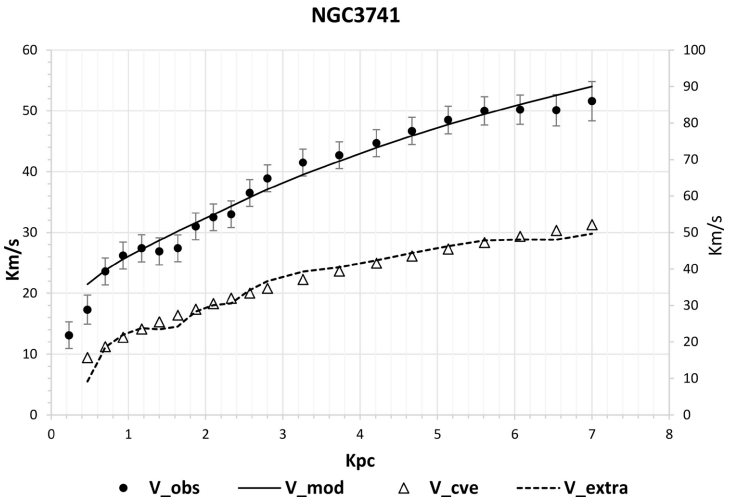

(a)

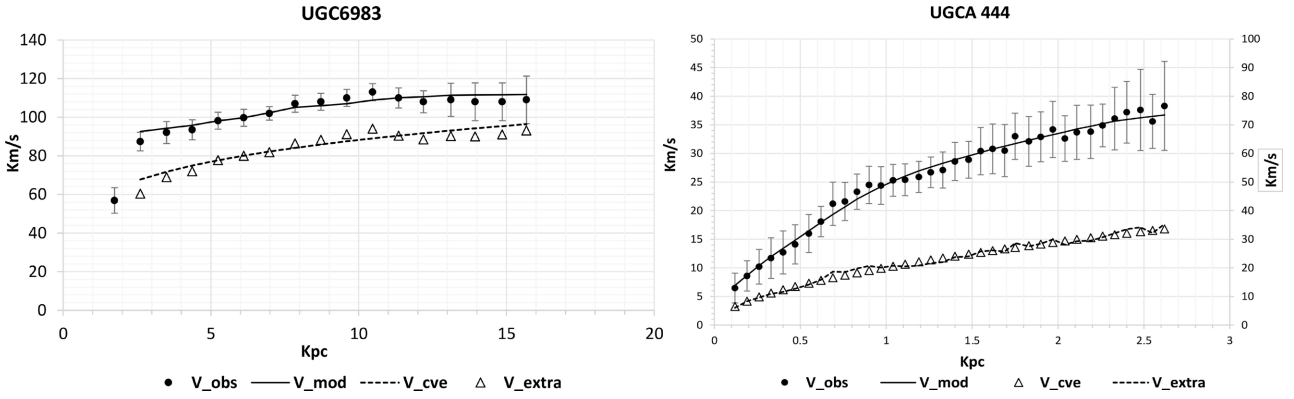

Figure 4. 4DEU rotation-curve fits for dwarf and low-surface-brightness (LSB) galaxies. NGC 3741 is curvature-dominated at all radii: the baryonic term remains small, while v_{extra} is large from the inner disk outward, and the model reproduces the steadily rising curve without tension. UGC 6983 shows a similar though less extreme behavior, with a smooth rise of both v_{extra} and v_{cve} across the disk. In contrast, UGCA444—an isolated dwarf irregular (dIrr) galaxy—exhibits a more balanced inner region where baryonic and curvature components contribute comparably, and the separation between v_{obs} and v_{bar} becomes significant only beyond the inner kiloparsec. Together, these galaxies illustrate the diversity of dwarf/LSB systems, from strongly curvature-dominated to nearly baryon-balanced disks.

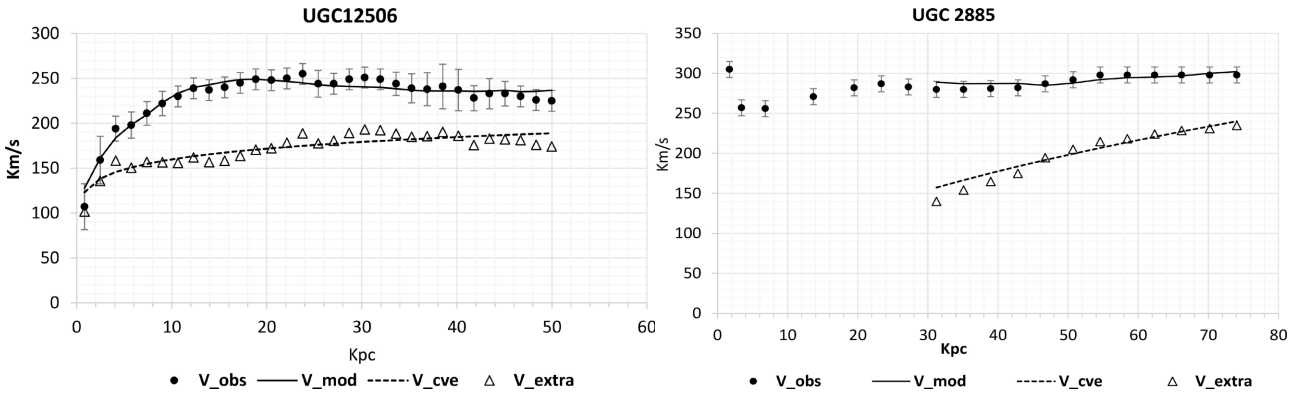

Figure 5. 4DEU rotation-curve fits for giant low-surface-brightness spiral galaxies. UGC 2885 and UGC 12506 extend to very large radii with diffuse stellar disks. Both exhibit high outer velocities sustained over tens of kiloparsecs; the 4DEU fits reproduce the gentle outer trends and the gradual strengthening of the **curvature-induced component** with radius. These giant systems illustrate the model's ability to describe extended, low-surface-brightness disks where the outer kinematics provide strong constraints on the fit parameters.

Declining Profiles ($\varepsilon < 0$) (Figure 6). UGC02916 and NGC7793 show mild outer declines, well fitted with negative ε. These cases serve as *control examples*: they confirm that the 4DEU model does not impose rising curves but accurately follows the observed trend toward the baryonic regime.

In both galaxies, the negative slope corresponds to the nearly Newtonian limit where the local blocking of local 3D expansion is only partial. Minor observational factors—such as outer-disk warps, pressure support, or non-circular motions—may further contribute to the gentle outer decrease, far from a Keplerian fall-off (see Section 6.2).

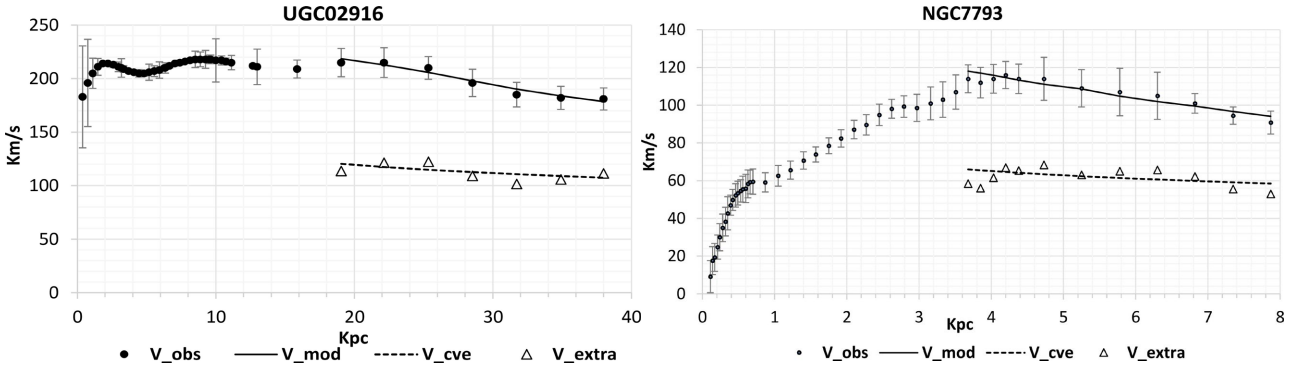

Figure 6. 4DEU rotation-curve fits for galaxies showing negative curvature slopes ($\varepsilon < 0$). **UGC02916:** in the SPARC data, v_{extra} is numerically undefined (negative radicand) up to ≈20 kpc, indicating a predominantly baryonic inner region; only beyond this radius does a weak curvature-induced component appear, with a mildly negative best-fit slope ($\varepsilon < 0$) consistent with the slowly declining v_{obs}. **NGC7793:** shows a similar qualitative pattern, with v_{extra} absent within the inner ≈2.5 kpc and a shallow outer decline fitted by $\varepsilon < 0$.

Non-Consistent Case (Figure 7). UGC05764, a faint LSB dwarf with irregular morphology, is the only galaxy with $p_{\text{gof}} < 0.01$. The model slightly overpredicts the outermost points, where increased scatter and large uncertainties inflate χ^2. As discussed in Section 6.2, this reflects observational limitations rather than a physical failure of the model; the positive $\varepsilon = 0.643 \pm 0.066$ still indicates an active local blocking of 3D expansion producing the curvature-induced velocity component.

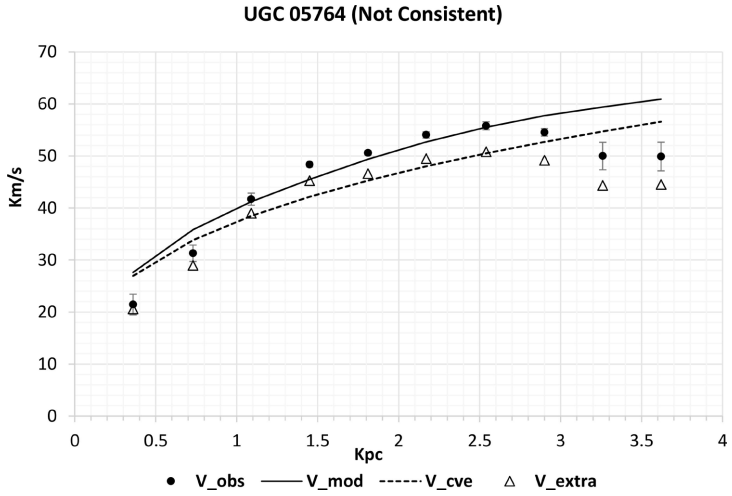

Figure 7. 4DEU fit for the galaxy UGC05764 (classified as "Not Consistent"). The outermost data points are slightly underpredicted by the model; their large scatter and measurement uncertainties inflate the χ^2 value, resulting in the low goodness-of-fit probability discussed in the text. This mismatch likely reflects observational limitations rather than a physical failure of the 4DEU law.

6.4. Global Behavior of the Fitted Parameters

The statistical analysis below includes the **128 galaxies** that satisfy the adopted

goodness-of-fit criterion ($p_{\text{gof}} \geq 0.01$); the only non-consistent case, **UGC05764**, is excluded from the computation of mean values because its fit does not meet the required significance level.

The **weighted-mean parameters**, obtained using the individual uncertainties as statistical weights, are:

$$\langle \varepsilon \rangle = 0.64 \pm 0.34; \qquad \langle V_0 \rangle = 47 \pm 24 \text{ km} \cdot \text{s}^{-1}$$

with a mean goodness-of-fit probability of:

$$\langle p_{\text{gof}} \rangle \simeq 0.94$$

These weighted averages quantify the **global statistical stability** of the 4DEU fits across the SPARC sample.

They demonstrate that the parameters are well constrained and physically consistent, confirming that the curvature-induced velocity component is typically flat or mildly rising in the domain where the extra velocity component dominates.

A few systems exhibit negative values of ε, corresponding to mildly declining profiles that have been described in Section 6.2.

Overall, the 4DEU formulation reproduces the entire diversity of galactic rotation curves, from giant spirals to faint dwarfs, using only the two physically defined parameters V_0 and ε, without invoking any additional matter component.

Statistically, the results confirm that 3-D spatial curvature generated by the gravitational constraint is sufficient to explain the observed galactic dynamics across the SPARC sample.

6.5. Global Outcome

The complete analysis of the SPARC sample demonstrates that **galactic rotation curves can be quantitatively reproduced without dark matter**, through the curvature of the 3-D spatial hypersurface generated by the gravitational constraint that locally blocks the 3D-only cosmic expansion. The 4DEU formulation captures this mechanism using only two parameters, V_0 and ε, which jointly describe the amplitude and local slope of the curvature-induced velocity. Their observed distributions, the excellent goodness-of-fit statistics, and the consistent representation of all main morphological categories (**Figures 2-6**) confirm the **statistical and physical consistency of the 4DEU framework** across the entire SPARC dataset.

7. Discussion and Conclusions

The results presented in Section 6 demonstrate that the velocity law derived from the ***Gravitational Constraint that Locally Blocks Expansion*** (GCLBE), expressed by Equation (12), reproduces the rotation curves of 128 out of 129 SPARC galaxies analyzed. In the following, we analyze the physical interpretation and broader implications of these findings.

Within the SPARC catalogue, the observed rotation curves can be quantitatively reproduced within the 4DEU theoretical framework without invoking any form of dark matter. For the vast majority of the 129 statistically eligible galaxies, the best-fit models yield $p_{\text{gof}} > 0.01$ and $\varepsilon > 0$, indicating that their outer rotation curves are slightly rising and consistent with a nearly complete local blocking (*i.e.*, within each galaxy) of the **3D component of the 4D cosmic expansion within each galaxy analyzed.**

Only two galaxies (NGC7793 and UGC02916) exhibit $\varepsilon < 0$, corresponding to weakly declining curves that approach the Newtonian-baryonic regime.

All fits were performed **exclusively in the domain where the extra velocity component dominates** the rotation curves—namely, where the baryonic contribution becomes subdominant.

This choice isolates the geometric component of curvature arising from the gravitational constraint, ensuring that the derived parameters V_0 and ε characterize the intrinsic 3D curvature rather than the local baryonic potential.

From a statistical perspective, the distribution of p-values confirms the robustness of the two-parameter equation yielding statistically consistent fits across the sample:

$$v_{\text{cve}}(r) = V_0 \left(\frac{r}{R_{\text{ref}}} \right)^{\varepsilon/2}$$

which accurately reproduces the kinematics **of the outer regions of galaxies** across the sample.

For nearly all galaxies, the fits yield $\varepsilon > 0$, corresponding to mildly rising profiles. In terms of effective density, this means that the curvature-generated component falls off more gently with radius, remaining higher in the analyzed radial domain than the r^{-2} profile expected for a perfectly flat curve.

Importantly, this behavior is **not imposed by the model** but directly reflects the observed trend of the data, which show, for the majority of the galaxies analyzed, a slight increase in both the observed and extra rotational velocities within the fitted radial domain (see **Figures 2-6** and Supplementary Data in [26]).

The 4DEU kinematic law (Equation (12)) naturally reproduces the observed behavior through the progressive strengthening of local 3D curvature, without invoking any additional dark component. The agreement between observed and modeled velocities further supports the interpretation that the apparent excess of rotational velocity arises from intrinsic **3D spatial curvature** generated by the gravitational constraint that locally suppresses the 3D-only cosmic expansion.

The effective curvature and the corresponding **3D Ricci scalar** inferred from the fitted profiles are consistent with the dynamical densities within the analyzed radial domains, reinforcing the geometric origin of the phenomenon.

Furthermore, the 4DEU framework remains fully consistent with **all classical weak-field tests of General Relativity**—including gravitational redshift, light deflection, Shapiro time delay, and Mercury's perihelion precession—since in 4DEU

these effects arise exclusively from spatial curvature, while the real-time (fourth-dimension) component remains perfectly flat [16].

This shows that **spatial curvature alone**, without any temporal curvature or spacetime warping, is sufficient to reproduce both the weak-field relativistic phenomena and the galactic-scale dynamics described by the parameters V_0 and ε.

Within this unified 4DEU framework, the same four-dimensional geometry that reproduces the observed H(z) relation without invoking dark energy [15], the linear evolution of the CMB temperature [14] [17], and the advanced development of galaxies observed at $z>10$ [14], consistently explains the kinematic behavior of nearby galaxies ($z\approx 0$) included in the SPARC sample through a single, parameter-free mechanism based on spatial curvature, as demonstrated in the present work. No additional components such as cold dark matter or dark energy are required, neither on cosmological, galactic, nor local scales.

Possible residual discrepancies can be attributed to observational uncertainties in baryonic mass estimates—mainly due to variations in the mass-to-light ratio—and to structural effects such as disk warps or non-circular motions not captured by the axisymmetric approximation.

Nevertheless, the adopted 25% systematic uncertainty on baryonic components effectively incorporates these effects, yielding statistically consistent fits across the sample.

It is worth noting that the phenomenology commonly attributed to dark matter, including galaxy rotation curves, has also been explored within the broader class of extended gravity frameworks (e.g., [31]).

Alternative frameworks such as MOND, $f(R)$ gravity, and the recent CCC + TL cosmology [32] reproduce flat galaxy rotation curves by introducing empirical parameters (e.g., MOND's a_0), metric modifications, or variable coupling constants (e.g., a tunable α) specifically adjusted to match the data. In contrast, 4DEU explains the same phenomenology as a direct geometric effect: the excess velocity arises from the purely spatial curvature of the 3D portion of the real 4D universe where we live, where gravitational binding locally blocks the 3D expansion. No variable constants, modified dynamics, or ad hoc tunings are required—flat or mildly rising outer rotation curves follow as a predictive consequence of the model's intrinsic geometry, rather than from externally imposed corrections.

Overall, this study supports the interpretation that the apparent dark halos of galaxies arise from 3D spatial curvature induced by the gravitational constraint that locally blocks the 3D-only cosmic expansion.

The 4DEU theoretical framework provides a coherent and observationally supported description of cosmic dynamics, being fully consistent with both relativistic weak-field limits and large-scale cosmological observations [16]. Within this context, the present analysis shows that the same framework quantitatively reproduces galactic rotation curves using only two parameters, V_0 and ε, with no need for dark matter.

Among the 129 statistically eligible SPARC galaxies, only **UGC05764** does not

satisfy the adopted goodness-of-fit criterion ($p_{\text{gof}} < 0.01$). Although its fitted parameters, $\varepsilon = 0.643 \pm 0.066$ and $V_0 \simeq 43.9\ \text{km/s}$, remain physically plausible and comparable to those of other low-mass systems, the high value of $\chi^2 = 35.87$ for $d.o.f = 8$ indicates a local mismatch between the curvature-based model and the observed velocities at the outermost radii.

This discrepancy can be traced to **two observational causes**, clearly visible in the SPARC rotation curve of this galaxy, as shown in Figure 7:

(1) Increased scatter of the outermost data points, where observational uncertainties on v_{obs} become large while the baryonic contribution is already negligible.

In logarithmic space, these points acquire high statistical weight, thus inflating χ^2 even for modest residuals. In the adopted weighted least-squares (WLS) scheme, the statistical weights scale approximately as $w_i \simeq \left(v_i/\sigma_{v,i}\right)^2$; consequently, outer points with large v_i can dominate the χ^2 budget even when their absolute uncertainties are significant.

(2) Possible non-circular motions or disk asymmetries. UGC05764 is a faint, low-surface-brightness (LSB) dwarf galaxy with irregular morphology and uncertain inclination. Residual warps or asymmetric gas motions can distort the observed velocity field, producing departures from the ideal axisymmetric assumption used in the fit.

In practice, **both effects may act simultaneously**, as LSB dwarfs frequently exhibit irregular gas kinematics and large measurement uncertainties in their outer regions. This combination leads to a formally low goodness-of-fit probability ($p_{\text{gof}} < 0.01$), classifying the galaxy as "Not Consistent" within the adopted statistical criterion. The localized overprediction of v_{mod} at large radii, visible in Figure 7, is most likely the main source of this $\Delta\chi^2$ excess.

From a physical standpoint, the fitted $\varepsilon > 0$ still implies that the **local blocking of 3D expansion** is active and that the curvature-induced velocity component $v_{\text{cve}}(r)$ increases mildly with radius, according to the 4DEU law

$$v_{\text{cve}}(r) = V_0 \left(\frac{r}{R_{\text{ref}}} \right)^{\varepsilon/2}$$

However, the large scatter of the observed data prevents a statistically consistent match within the adopted baryonic uncertainty of ±25%. Therefore, the classification *Not Consistent* for UGC 05764 does not falsify the model: it simply reflects the **limited quality of the observational data**, rather than any failure of the underlying 4DEU kinematic law.

The proposed interpretation also provides a natural explanation for the observed diversity among dwarf galaxies. Within the 4DEU theoretical framework, the spatial curvature, responsible for the observational effects that in ΛCDM are attributed to dark matter, increases over cosmic time as a direct consequence of the gravitational constraint, which progressively strengthens and prevents the separation of masses that would otherwise occur due to the global expansion. Conse-

quently, the older a galaxy is, the greater the amount of accumulated spatial curvature, and thus the higher its apparent dark-to-baryonic matter ratio—reaching about 90% in the oldest dwarf systems [33] and up to several hundred in the most dark-matter-dominated ultra-faint dwarfs such as Segue 1 [34]-[36]. This trend is consistent with recent studies confirming that ultra-faint dwarf galaxies are among the oldest known systems and exhibit extremely high mass-to-light ratios [36]-[38]. However, there also exist cases of dwarf galaxies apparently lacking dark matter. These can be interpreted, in the same 4DEU context, as systems undergoing the disruption or loss of their gravitational constraint due to strong external tidal interactions from nearby massive galaxies. The absence of the effective "extra" component would then reflect the partial disappearance of the spatial curvature that once maintained their internal equilibrium [39] [40].

Data Availability

The complete per-galaxy fit tables are publicly available as an Excel workbook with one worksheet per galaxy. The dataset is available as *Supplementary Material* under the title *SPARC-4DEU per-single galaxy rotation-curve fits* on Zenodo [26].

Additional Supplementary Excel files containing the full fitting results obtained at the two alternative dominance thresholds ($v_{\text{extra}}/v_{\text{obs}} \geq 0.05$ and $v_{\text{extra}}/v_{\text{obs}} \geq 0.707$) are also available at https://doi.org/10.5281/zenodo.17559295.

Acknowledgements

The author wishes to express gratitude to **Dr. Massimiliano Florio**, President of the pharmaceutical company **Special Product's Line, Italy**, for the indirect support provided in the development of the present work.

Conflicts of Interest

The authors declare no conflicts of interest regarding the publication of this paper.

References

[1] Sofue, Y. and Rubin, V. (2001) Rotation Curves of Spiral Galaxies. *Annual Review of Astronomy and Astrophysics*, **39**, 137-174. https://doi.org/10.1146/annurev.astro.39.1.137

[2] Lelli, F., McGaugh, S.S. and Schombert, J.M. (2016) SPARC: Mass Models for 175 Disk Galaxies with Spitzer Photometry and Accurate Rotation Curves. *The Astronomical Journal*, **152**, Article 157. https://doi.org/10.3847/0004-6256/152/6/157

[3] Lelli, F., McGaugh, S.S. and Schombert, J.M. (2016) SPARC Galaxy Rotation Curve (Dataset). Zenodo.

[4] Clowe, D., Bradač, M., Gonzalez, A.H., Markevitch, M., Randall, S.W., Jones, C., *et al.* (2006) A Direct Empirical Proof of the Existence of Dark Matter. *The Astrophysical Journal*, **648**, L109-L113. https://doi.org/10.1086/508162

[5] Bartelmann, M. and Schneider, P. (2001) Weak Gravitational Lensing. *Physics Reports*, **340**, 291-472. https://doi.org/10.1016/s0370-1573(00)00082-x

[6] Mandelbaum, R. (2018) Weak Lensing for Precision Cosmology. *Annual Review of*

Astronomy and Astrophysics, **56**, 393-433.
https://doi.org/10.1146/annurev-astro-081817-051928

[7] Planck Collaboration (2020) Planck 2018 results. VI. Cosmological Parameters. *Astronomy & Astrophysics*, **641**, 67 p.

[8] Bertone, G. and Tait, T.M.P. (2018) A New Era in the Search for Dark Matter. *Nature*, **562**, 51-56. https://doi.org/10.1038/s41586-018-0542-z

[9] Particle Data Group (2024) Review of Particle Physics. *Progress of Theoretical and Experimental Physics*, **110**, Article 083C01.

[10] Schumann, M. (2019) Direct Detection of WIMP Dark Matter: Concepts and Status. *Journal of Physics G: Nuclear and Particle Physics*, **46**, Article 103003.
https://doi.org/10.1088/1361-6471/ab2ea5

[11] XENONnT Collaboration (2023) Dark Matter Search Results from XENONnT. *Physical Review Letters*, **131**, Article 041002.

[12] LZ Collaboration (2023) First Dark Matter SEARCH Results from the LUX-ZEPLIN (LZ) Experiment. *Physical Review Letters*, **131**, Article 041001.

[13] Maglione, D. (2024) Theory of the Four-Dimensional Electromagnetic Universe, Part I: A Real Hyperspherical Four-Dimensional Universe Can Explain the Equations E = hf and E = mc^2, As Well As the Wave-Particle Duality of Electro-Magnetic Waves. *Journal of Physics and Astronomy*, **12**, Article 397.

[14] Maglione, D. (2025) Theory of the Four-Dimensional Electromagnetic Universe (4DEU): Temporal Waves as the Origin of the Universe's Creation, Expansion, and Gravitation. Eliva Press.

[15] Maglione, D. (2025) Hubble Parameter Evolution in the 4DEU Framework: No Need for Dark Energy and Implications for the Hubble Tension. *Journal of High Energy Physics, Gravitation and Cosmology*, **11**, 1499-1515.
https://doi.org/10.4236/jhepgc.2025.114092

[16] Maglione, D. (2025) Gravitation in the Theory of the Four-Dimensional Electromagnetic Universe (4DEU): Weak-Field Relativistic Effects from Spatial Curvature Alone. *Advances in Theoretical & Computational Physics*, **8**, 1-26.
https://doi.org/10.33140/atcp.08.03.05

[17] Maglione, D. (2024) Theory of the Four-Dimensional Electromagnetic Universe, Part II: Temporal Waves as the Foundation of the Creation and Expansion of the Universe. *Journal of Modern Applied Physics*, **7**, 1-17.

[18] Muller, S., Beelen, A., Black, J.H., Curran, S.J., Horellou, C., Aalto, S., *et al.* (2012) A Precise and Accurate Determination of the Cosmic Microwave Background Temperature at Z = 0.89. *Astronomy & Astrophysics*, **551**, A109.
https://doi.org/10.1051/0004-6361/201220613

[19] Molaro, P., Levshakov, S.A., Dessauges-Zavadsky, M. and D'Odorico, S. (2002) The Cosmic Microwave Background Radiation Temperature at Z = 3.025 toward QSO 0347-3819. *Astronomy & Astrophysics*, **381**, L64-L67.
https://doi.org/10.1051/0004-6361:20011698

[20] Riechers, D.A., Weiss, A., Walter, F., Carilli, C.L., Cox, P., Decarli, R., *et al.* (2022) Microwave Background Temperature at a Redshift of 6.34 from H_2O Absorption. *Nature*, **602**, 58-62. https://doi.org/10.1038/s41586-021-04294-5

[21] Oesch, P.A., Brammer, G., Dokkum, P.G.v., Illingworth, G.D., Bouwens, R.J., Labbé, I., *et al.* (2016) A Remarkably Luminous Galaxy at Z = 11.1 Measured with Hubble Space Telescope GRISM Spectroscopy. *The Astrophysical Journal*, **819**, 129-140.
https://doi.org/10.3847/0004-637x/819/2/129

[22] D'Eugenio, F., Maiolino, R., Carniani, S., Chevallard, J., Curtis-Lake, E., Witstok, J., *et al*. (2024) JADES: Carbon enrichment 350 Myr after the Big Bang. *Astronomy & Astrophysics*, **689**, A152. https://doi.org/10.1051/0004-6361/202348636

[23] Carniani, S., Hainline, K., D'Eugenio, F., Eisenstein, D.J., Jakobsen, P., Witstok, J., *et al*. (2024) Spectroscopic Confirmation of Two Luminous Galaxies at a Redshift of 14. *Nature*, **633**, 318-322. https://doi.org/10.1038/s41586-024-07860-9

[24] Binney, J. and Tremaine, S. (2008) Galactic Dynamics, 2nd Edition, Princeton University Press.

[25] Arnowitt, R., Deser, S. and Misner, C.W. (2008) Republication of: The Dynamics of General Relativity. *General Relativity and Gravitation*, **40**, 1997-2027. https://doi.org/10.1007/s10714-008-0661-1

[26] Maglione, D. (2025) SPARC-4DEU Per-Single Galaxy Rotation-Curve Fits (Excel Workbook; [129/126] Worksheets, One Per Galaxy). Zenodo.

[27] Cohen, J. (1988) Statistical Power Analysis for the Behavioral Sciences. 2nd Edition, Lawrence Erlbaum Associates.

[28] McGaugh, S.S. and Schombert, J.M. (2014) Color-Mass-to-Light-Ratio Relations for Disk Galaxies. *The Astronomical Journal*, **148**, Article 77. https://doi.org/10.1088/0004-6256/148/5/77

[29] Bevington, P.R. and Robinson, D.K. (2003) Data Reduction and Error Analysis for the Physical Sciences. 3rd Edition, McGraw-Hill.

[30] William, W.H., Teukolsky, S.A., Vetterling, W.T. and Flannery, B.P. (2007) Numerical Recipes: The Art of Scientific Computing. 3rd Edition, Cambridge University Press.

[31] Corda, C. (2009) Interferometric Detection of Gravitational Waves: The Definitive Test for General Relativity. *International Journal of Modern Physics D*, **18**, 2275-2282. https://doi.org/10.1142/s0218271809015904

[32] Gupta, R.P. (2025) Testing CCC+TL Cosmology with Galaxy Rotation Curves. *Galaxies*, **13**, Article 108. https://doi.org/10.3390/galaxies13050108

[33] Chiti, A., Frebel, A., Ji, A.P., Jerjen, H., Kim, D. and Norris, J.E. (2018) Chemical Abundances of New Member Stars in the Tucana II Dwarf Galaxy*. *The Astrophysical Journal*, **857**, 74-87. https://doi.org/10.3847/1538-4357/aab4fc

[34] Frebel, A., Simon, J.D. and Kirby, E.N. (2014) Segue 1: An Unevolved Fossil Galaxy from the Early Universe. *The Astrophysical Journal*, **786**, Article 74. https://doi.org/10.1088/0004-637x/786/1/74

[35] Xiang-Gruess, M., Lou, Y. and Duschl, W.J. (2009) Dark Matter Dominated Dwarf Disc Galaxy Segue 1. *Monthly Notices of the Royal Astronomical Society: Letters*, **400**, L52-L56. https://doi.org/10.1111/j.1745-3933.2009.00761.x

[36] Simon, J.D. (2019) The Faintest Dwarf Galaxies. *Annual Review of Astronomy and Astrophysics*, **57**, 375-415. https://doi.org/10.1146/annurev-astro-091918-104453

[37] Revaz, Y. (2023) The Compactness of Ultra-Faint Dwarf Galaxies: A New Challenge? *Astronomy & Astrophysics*, **679**, A2. https://doi.org/10.1051/0004-6361/202347239

[38] Alexander, R.K., Vincenzo, F., Ji, A.P., Richstein, H., Jordan, C.J. and Gibson, B.K. (2023) Inhomogeneous Galactic Chemical Evolution: Modelling Ultra-Faint Dwarf Galaxies of the Large Magellanic Cloud. *Monthly Notices of the Royal Astronomical Society*, **522**, 5415-5433. https://doi.org/10.1093/mnras/stad1312

[39] Shen, Z., Danieli, S., van Dokkum, P., Abraham, R., Brodie, J.P., Conroy, C., *et al*. (2021) A Tip of the Red Giant Branch Distance of 22.1 ± 1.2 Mpc to the Dark Matter Deficient Galaxy NGC 1052-DF2 from 40 Orbits of Hubble Space Telescope Imaging.

The Astrophysical Journal Letters, **914**, L12.
https://doi.org/10.3847/2041-8213/ac0335

[40] van Dokkum, P., Danieli, S., Abraham, R., Conroy, C. and Romanowsky, A.J. (2019) A Second Galaxy Missing Dark Matter in the NGC 1052 Group. *The Astrophysical Journal Letters*, **874**, L5. https://doi.org/10.3847/2041-8213/ab0d92

Appendix A. Alternative Model-Independent Derivation from Gauss's Law

Independently of the specific theory, in spherical symmetry the divergence of the gravitational acceleration field $\vec{g}(r) = g_r(r)\hat{r}$ is:

$$\nabla\vec{g} = \frac{1}{r^2}\frac{\mathrm{d}}{\mathrm{d}r}\left[r^2 g_r(r)\right] \tag{A1}$$

Using Gauss's law in differential form,

$$\nabla\vec{g} = 4\pi G\,\rho_{eff}(r) \tag{A2}$$

and the kinematic identity for circular orbits,

$$g_r(r) = \frac{v^2(r)}{r} \tag{A3}$$

we obtain the general link between the observed rotation curve and the corresponding effective density:

$$\rho_{\mathrm{eff}}(r) = \frac{1}{4\pi G r^2}\frac{\mathrm{d}}{\mathrm{d}r}\left[r\,v^2(r)\right] \tag{A4}$$

that is exactly the Equation (3) described in Section 2.

Expanding the derivative gives:

$$\rho_{\mathrm{eff}}(r) = \frac{1}{4\pi G r^2}\left[v^2(r) + 2r\,v(r)\frac{\mathrm{d}v(r)}{\mathrm{d}r}\right] \tag{A5}$$

Equation (A5) is purely kinematic and model independent.

For a perfectly flat curve ($\mathrm{d}v/\mathrm{d}r \simeq 0$) it reduces to the isothermal-like profile

$$\rho_{\mathrm{eff}}(r) \simeq \frac{V_{0,\mathrm{tot}}^2}{4\pi G r^2} \tag{A6}$$

where $V_{0,\mathrm{tot}}$ is the asymptotic plateau of the total observed velocity $v_{\mathrm{obs}}(r)$.